Journal of Materials Chemistry C

Accepted Manuscript

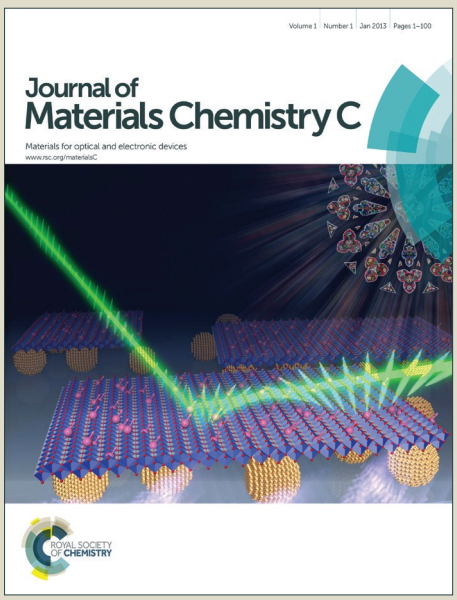

ROYAL SOCIETY OF CHEMISTRY

www.rsc.org/materialsC

Structure and electrical properties of layered perovskite type $Pr_2Ti_2O_7$: Experimental and theoretical investigations

Sadequa J. Patwe,[1] Vasundhara Katari,[1] Nilesh P. Salke,[2] Sudhanshu K. Deshpande,[3] Rekha Rao,[2] Mayanak K. Gupta,[2] Ranjan Mittal,[2] S. Nagabhusan Achary,[1] * and Avesh K. Tyagi[1] *

[1] *Chemistry Division, Bhabha Atomic Research Centre, Mumbai 400085, India*

[2] *Solid State Physics Division, Bhabha Atomic Research Centre, Mumbai 400085, India*

[3] *UGC-DAE Consortium for Scientific Research, BARC, Mumbai 400085, India*

Abstract: *In this communication we report details of structure and thermal properties of monoclinic layered perovskite type $Pr_2Ti_2O_7$ (PTO) from ambient to higher temperature XRD and Raman spectroscopic studies. The monoclinic ($P2_1$) structure is found to be the stable structure of PTO compared to the orthorhombic $Pna2_1$, $Cmc2_1$ or Cmcm and monoclinic $P2_1/m$ structures. The crystal structure is further supported from the ab-initio total energy calculations by using density functional theory (DFT) formalism. The total energy calculation and structural relations favour for the ferroelectric ($P2_1$) to paraelectric ($P2_1/m$) displacive transition. The calculated electric polarization as observed from the displacement of ions is ~ 8.3 $\mu C/cm^2$. The calculated electron density of states indicated a band gap of about 2.7 eV, which closely agrees with that measured by UV-Vis diffuse reflectance spectroscopy. Variable temperature XRD and differential thermal analyses studies revealed no structural transition to $Cmc2_1$ in the temperature range from ambient to 1473 K as reported for analogous rare-earth titanates, like $La_2Ti_2O_7$ and $Nd_2Ti_2O_7$. A partial decomposition of PTO to cubic perovskite type structure is observed at around 1673 K. The measurement of field dependent electric polarization indicates the ferroelectric nature of PTO. The electrical properties of PTO have also been investigated by ac impedance spectroscopic studies from 173 to 1073 K. The low temperature dielectric data indicate two different types of relaxations, one at lower frequency region and strongly*

temperature dependent while the other at higher frequency (>1 kHz) and nearly temperature independent. The low and high frequency relaxations have been attributed to the thermally activated polarization process arising from the grain boundaries and dipolar orientations, respectively. The activation energy for thermally activated low frequency relaxation process is 0.38 eV, which is similar to the interfacial polarizations due to ionic movements. Appreciable contribution of ionic conductivity in PTO is observed at still higher temperature (~ 700 K). The activation energy for ionic conductivity is about 0.60 eV.

Key words: Layered perovskite, Titanate, Ferroelectric, Dielectric, Crystal structure, DFT

*** Corresponding Authors:**

Dr. S. N. Achary
Chemistry Division, Bhabha Atomic Research Centre, Mumbai, 400 085, INDIA
Phone: 0092-22-25592328; Fax: 0091-22-25505151
E-mail: sachary@barc.gov.in; acharysn@rediffmail.com

Dr. A. K. Tyagi
Chemistry Division, Bhabha Atomic Research Centre, Mumbai, 400 085, INDIA
Phone: 0092-22-25592328; Fax: 0091-22-25505151
E-mail: aktyagi@barc.gov.in

1. INTRODUCTION

$A_2B_2O_7$ type compositions with A = trivalent rare-earth ions and B= tetravalent ions, like Ti^{4+}, Zr^{4+}, Hf^{4+} and Sn^{4+}, have been of interest due to their interesting crystal chemistry and several technological applications based on their dielectric, ferroelectric and piezoelectric as well as ionic conductivity. Depending on the radius of the cations, the $A_2B_2O_7$ type compositions of rare-earth ions can be grouped into three categories, namely, (a). fluorite ($r_A/r_B < 1.48$), (b). pyrochlore ($1.48 < r_A/r_B < 1.78$) and (c). perovskite ($r_A/r_B > 1.78$) structure types. [1,2] For Ti^{4+} as B site cation, the $A_2B_2O_7$ type rare-earth (Ln) titanates form monoclinic perovskite type structure for A = La, Nd and Pr while all others form cubic pyrochlore type structures. [3] The monoclinic perovskite type titanates have been of attraction due to their high Curie temperature ferroelectric and piezoelectric properties, high dielectric constants, nonlinear optical and photocatalyic properties. [4-12] Early studies on phase diagrams in Ln_2O_3-TiO_2 systems by Shcherbakova et al. [3] had revealed that both monoclinic or cubic $Ln_2Ti_2O_7$ phases have higher melting temperature (>1450°C). Nanamatsu et al. [6] have reported ferroelectric and nonlinear optical activity in monoclinic $La_2Ti_2O_7$. From the high temperature dielectric studies, Yan et al. [4] have suggested that the ferroelectric to paraelectric transition temperature of $La_2Ti_2O_7$ and $Nd_2Ti_2O_7$ is above 1073 K. It has been reported that the octahedral network and interstitial cations of $Ln_2Ti_2O_7$ play a significant role in their electronic as well as dielectric properties. [11,13-15]

Despite the structural similarity in all the three compositions, viz. $A_2Ti_2O_7$ (A = La, Nd and Pr), much research attention has been devoted to $La_2Ti_2O_7$ or $Nd_2Ti_2O_7$ while the $Pr_2Ti_2O_7$ is still under explored. Among the monoclinic rare-earth titanates $Pr_2Ti_2O_2$ and $Ce_2Ti_2O_7$ are likely to have exceptional behaviour due to intrinsic defects arising from the variable valence states of Pr and Ce. Recently, Atuchin et al. [16] have reported spectroscopic and electronic properties of $Pr_2Ti_2O_7$. Investigations on optical and dielectric properties of $Pr_2Ti_2O_7$ indicate larger non-linear optical activity and dielectric constant of about 27–32. [13] Literature also shows the ferroelectric transition of $Pr_2Ti_2O_7$ depends on the nature of sample preparation. The ferroelectric transition around 740°C has been reported in the spark plasma sintered sample of $Pr_2Ti_2O_7$. [7] Sun et al. have reported coupled magnetism and ferroelectric properties in nanocrystalline $Pr_2Ti_2O_7$, where the magnetism is associated to the oxygen vacancies while the

ferroelectricity has been assigned to the structural features. [17] The frequency and temperature dependent dielectric studies of Sun et al. [17] indicated an anomaly near the suggested ferroelectric transition temperature (570 K) and the lowering of Tc has been claimed for the crystallite size effects. This value of reported transition temperature for $Pr_2Ti_2O_7$ is the lowest temperature reported for any of the monoclinic $Ln_2Ti_2O_7$ phases. [3,4,7,17]

Though such titanates have been of technological importance, their structure and phase transitions are still obscure in literature. The structure of $Ln_2Ti_2O_7$ (Ln = La and Nd) has been explained by a monoclinic ($P2_1$) lattice. [3,18-20] However, a closely related orthorhombic ($Pna2_1$) has also been assigned for the structure of $La_2Ti_2O_7$. [21,22] In addition Scheunemann & Müller-Buschbaum [22] and Harvey et al. [23] have reported a monoclinic super-structure with $P2_1$ symmetry for exact crystal structure of $Nd_2Ti_2O_7$. High temperature structural studies on $La_2Ti_2O_7$ indicate a structural transition from $P2_1$ to $Cma2_1$ above 1053°C and both low and high temperature phases differ by the shift of the rare-earth ions as well as distortion and tilt of the TiO_6 octahedral units. [24] From the structural analyses the authors have indicated that the polarization in these structures arises mainly from shift of the rare-earth ions and partly from the rotation of the deformed TiO_6 octahedra. Recently, Ishizawa et al. [25] have investigated the crystal structure of $Nd_2Ti_2O_7$ and indicated that the sub-cell represents the actual structure of $Nd_2Ti_2O_7$ which is related to the earlier reported super-structure by the differences in shift of cations along one of the axes, i.e. along the polarization direction. From density functional calculations, Pruneda et al. [26], Zhang et al. [27] and Xioa et al. [28] have reported structure and elastic properties of cubic phase of $La_2Ti_2O_7$ and $Nd_2Ti_2O_7$, while such cubic phases have never been observed experimentally. Theoretical analysis of Lopez-Perez and Iniguez [15] indicated that the transformation from $Cmc2_1$, the real high temperature structure of $La_2Ti_2O_7$ to paraelectric (Cmcm) structure is related to the shift of cations and distortion of octahedra and is a topological ferroelectric transition. [15] Similar studies on $La_2Ti_2O_7$ and $Nd_2Ti_2O_7$ by Bruyer and Sayede [14] indicated that the monoclinic ($P2_1$) structure is the stable phase at ambient condition. This study also indicates that the transformation from ferroelectric to paraelectric phase may occur as $P2_1$ to $P2_1/m$ structural transition. However, the prototype $P2_1/m$ or Cmcm phases have never been observed experimentally for any of these titanates up to melting temperature. Besides these studies there are no other reports available in literature to confirm the dielectric properties as well as high temperature structural properties of $Pr_2Ti_2O_7$. In view of this we have prepared

$Pr_2Ti_2O_7$ and investigated the structure and electrical properties in wider range of temperature and frequency.

2. EXPERIMENTAL

The polycrystalline sample of $Pr_2Ti_2O_7$ was prepared by solid state reaction of appropriate amounts of Pr_6O_{11} and TiO_2. Pr_6O_{11} was preheated at 1073 K to remove any adsorbed moisture. TiO_2 was heated at 1273 K to remove any adsorbed moisture or hydroxyl groups. About 7 g of the homogenous mixture was prepared by mixing stoichiometric amounts of the reactants in acetone media. The mixed powder was pressed into pellets (about 1 inch diameter and 5 mm height) and slowly heated to 1173 K and held for 24 h. The pellet obtained after cooling to room temperature was rehomogenized and heated at 1373 K for another 24 h. The completion of the reaction is ensured after this heating step. The pellet is then rehomogenized and then pressed into pellets of about 1 cm diameter and 2 mm height. These pellets were sintered at 1573 K for 24 h and cooled at the rate of 2 K/min to ambient temperature. Well sintered pellets obtained after this heat treatment were used for all the studies.

The product obtained after final sintering step was characterized by powder XRD data recorded on a rotating anode based X-ray diffractometer (Ragaku, Japan). Powder sample of $Pr_2Ti_2O_7$ was pressed into a groove of about 1 mm of a glass sample holder and XRD data were collected from 5 to 100° with step width of 0.02° and time per step is 5 sec. The XRD patterns at several temperatures in between ambient to 1000°C were recorded on a powder X-ray diffractometer (X-pert Pro Panalytical) equipped with Anton Parr high temperature attachment. Well ground sample was smeared on a platinum strip sample holder-cum-heater. The sample is heated to a desired temperature at a rate of 20 K/min and held for 5 m for equilibration. The HT-XRD patterns were recorded in the two-theta range of 10-80° with step width and step time as 0.02° and 1.5 s, respectively. Monochromatized Cu-Kα radiation was used for recording the XRD data at ambient and higher temperature. The powder XRD data were analyzed by Rietveld refinement method using *GSAS* and *Fullprof 2000* software packages. [29,30]

Raman spectroscopic measurements in the temperature range of 298–1073 K were carried out by using the Linkam variable temperature stage (Model-TS 1500) in back-scattering geometry. Spectrum of polycrystalline sample of $Pr_2Ti_2O_7$ was excited using 532 nm laser line

with power 15 mW. Scattered light was analyzed by using a home built 0.9 m single monochromator, coupled with an edge filter and detected by a cooled CCD. [31] Entrance slit was kept at 50 µm, which gives a spectral band pass of 3 cm^{-1}.

Thermal stability and oxidation behavior of the sample in dry oxygen and argon were studied by simultaneous thermogravimetric (TG) and differential thermal analyses (DTA) method. The TG and DTA traces were recorded while heating about 100 mg of sample to 1673 K on a thermobalance (SETARAM Instrumentation, France). Typical heating rate 10 K/min was used for recording the TG-DTA data. The residue obtained after the TG-DTA runs were also characterized by powder XRD study.

The microstructure of sintered samples was studied by using Scanning electron microscope (Zeiss, Gemany). The micrographs at different magnifications were recorded on both top and fractured surfaces of sintered pellets.

The electric field dependent electric polarizations (PE-loops) were recorded at ambient temperature by using Aixacct TF2000 (Aixacct GmbH, Germany) ferroelectric analyzer. Polarization data were recorded by using platinum paste coated pellets of sample (2 mm thickness).

UV–visible (*UV-Vis.*) diffuse reflectance spectrum was recorded on a two-beam spectrometer (V-670, JASCO) using fine powder sample.

For impedance measurements, platinum paste coated on two parallel faces of cylindrical pellets were used. The dielectric properties of the pellets were measured in a parallel-plate capacitor configuration using flat gold-plated electrodes. Low temperature (173 to 473 K) impedance measurements were carried out by using Novocontrol Alpha AN impedance analyzer (Novocontrol Technologies, Germany) and Quatro nitrogen cryosystem. The complex dielectric data were recorded at a series frequency range of 100 Hz to 5 MHz at several temperatures while heating from 173 K to 473 K. The electrical properties between 300and1073K were investigated by using an impedance analyzer (Solartron impedance analyzer, Model 1290). In both cases, *rms* bias voltage of 0.5 V was used for data collection. The impedance data were measured in the frequency range of 1MHz to 1 Hz at several temperatures while heating the sample. The dielectric and impedance data were analyzed by using *Winfit* and *Z-view* software packages.

3. DENSITY FUNCTIONAL CALCULATIONS

The total energy calculations for various structural models of $Pr_2Ti_2O_7$ have been carried out by using *ab-initio* density functional theory (DFT). The calculations were performed by using the projector-augmented wave formalism [32] of the Kohn-Sham formulation of the density-functional theory (DFT) [33,34] at the generalized gradient approximation (GGA) level, implemented in the Vienna *ab initio* simulation package (VASP). [35,36] The GGA was formulated by the Perdew-Burke-Ernzerhof (PBE) density functional approximations. [37,38] All results are well converged with respect to *k* mesh and energy cutoff for the plane-wave expansion. The total energy calculations have been carried out by using a cutoff of 820 eV of plane wave kinetic energy. K-points mesh was generated according to the Monkhorst-Pack (MP) scheme. [37-39] The break conditions for the self-consistent field and for the ionic relaxation loops were set to 10^{-8}eV $Å^{-1}$ and 10^{-4}eV $Å^{-1}$, respectively. The Hellmann-Feynman forces following the geometry optimization were less than 10^{-4}eV $Å^{-1}$. The numbers of valence electron used in oxygen, titanium and praseodymium atomic pseudo-potentials are 6, 4 and 11, respectively. Full geometry optimizations along with unit cell parameters were carried out on various structural models of $Pr_2Ti_2O_7$. The variation of energy with volume at 0 K and electron density of states *(dos)* was calculated for all the five relaxed structures.

4. RESULTS AND DISCUSSION

The observed reflections of the powder XRD data of $Pr_2Ti_2O_7$ (PTO) sample obtained after final sintering are quite similar to the reported monoclinic (JC-PDS-PDF: 35-0267) as well as orthorhombic (JC-PDS-PDF: 35-0224) phases. As mentioned in the introduction section the structure of PTO and analogous rare-earth titanates has been explained by diversified symmetries, viz. monoclinic ($P2_1$ and $P2_1/m$) and orthorhombic ($Pna2_1$, $Cmc2_1$ and Cmcm). The ferroelectric phase of PTO is likely to have $P2_1$, $Pna2_1$ or $Cmc2_1$ symmetry, while the paraelectric phase is likely to have monoclinic $P2_1/m$ or orthorhombic Cmcm symmetry. [20,21,24,32] It can be mentioned here that all the structures are closely related and hence their XRD patterns show only marginal differences. In order to elucidate the structure of PTO, we have considered

the reported structural details of monoclinic ($P2_1$) of PTO and orthorhombic ($Pna2_1$ and $Cmc2_1$) symmetries of $La_2Ti_2O_7$. Initial models for other structures were obtained by structural transformations as shown in **Figure-1**. Thus the Rietveld refinements of the powder X-ray diffraction (XRD) were carried by considering all the possible models based on $Ln_2Ti_2O_7$ and related structure types, viz. $P2_1$, $P2_1/m$. $Pna2_1$, $Cmc2_1$ and Cmcm symmetries. The peaks and background of the diffraction pattern were modeled by using pseudo-Voigt profile function and shifted Chebyschev polynomial function, respectively. Initially background parameters along with the scale were refined and unit cell parameters, half-width (U, V and W) and mixing (η) parameters of Pseudo-Voigt function and peak asymmetry corrections were added in the subsequent refinement cycles. All the intense peaks could be explained by any of the considered models. However the intensities of some weak peaks, in particular peaks at two theta ~ 35.0, 37.5°, favour for orthorhombic ($Pna2_1$) [21] and monoclinic ($P2_1$) [23] structures compared to the orthorhombic $Cmc2_1$ or Cmcm structures. [20] The refinement of the position coordinates of all the possible models were subsequently carried out to further ascertain the structure of PTO. The goodness of fit was monitored from the residual (R-values) of refinements and differences between the observed and calculated diffraction patterns. It can be mentioned here that the monoclinic unit cell reported by Scheunemann and Mueller-Buschbaum [22] and Harvey et al. [24] was also considered for refinements. The refinements with this monoclinic super-structure model indicate closely similar residuals while the unit cell parameter is doubled along the c-axis. Despite the structure consist of twice the number of atoms in asymmetric unit and has larger unit cell, no better residuals as well as profile could be obtained in the super-structure model of monoclinic $P2_1$ structure. Hence, this model was not considered for further study. Also, the $Pna2_1$ symmetry has larger unit cell parameters and should exhibit extra reflections as well as detectable intensity at $2\theta \sim 12.4$ and 23.5°. The present observed powder XRD pattern are not agreements with these aspects. Additionally, a weak peak observed at $2\theta \sim 14.4°$ is attributable only to $P2_1$ symmetry. Thus we support the monoclinic $P2_1$ structure as the actual structure of PTO.

The refined unit cell parameters and the residuals of the refinements with different structural models are summarized in **Table 1**. A comparison of the residuals obtained in different models indicates that the monoclinic ($P2_1$) structure with unit cell parameters: a = 7.7152(1), b = 5.4878(1), c = 13.0042(2) Å and β = 98.552(4)° is the best model for the observed diffraction data. The refined position coordinates and typical inter-atomic distances for the monoclinic ($P2_1$) structure are given in **Table 2** and **3**, respectively. The typical Rietveld refinement plot of the final cycle for $P2_1$ structure is shown in **Figure 2**.The refined structural parameters and Rietveld refinement plots for other considered models are provided as supplementary data (***Supplementary data S-I and II***) to this manuscript.

The analyses of the refined structural parameters of PTO at ambient temperature in $P2_1$ symmetry indicate that the structure has crystallographically distinguishable four Pr (Pr1 to Pr4) atoms, four Ti (Ti1 to Ti4) atoms and fourteen oxygen atoms. The typical crystal structure of PTO and its projection along the *a*- and *c*-axes are shown in **Figure 3 (a, b)**. All the TiO_6 octahedra of the PTO are distorted and connected by sharing the corners to form perovskite type octahedral net. However, the periodicity disrupts along the *c*-axis which render it to a layered structure. The interstices in the perovskite slabs are filled by the Pr1 and Pr2 atoms. The Pr3 and Pr4 are located closer to interlayer interstices. The shift of these atoms from the *ab*-plane causes a variation in the stacking of the perovskite slabs in the PTO structure. The transformation of perovskite to layered perovskites systems has been reported earlier in literature. [40] The excess oxygen contents compared to the stoichiometry of the perovskite composition cleave the octahedral connections and in turn lead to layered structures with $A_nB_nO_{3n+1}$ homologues. In the PTO structure, all the Ti atoms (Ti1, Ti2, Ti3 and Ti4) have octahedral coordination with the anions with Ti-O bond lengths in between 1.83 to 2.25 Å, while the Pr^{3+} ions are 10 (Pr1, Pr2) or 8 (Pr3 and Pr4) coordinated with the oxygen atoms. The Pr^{3+} ions inside the perovskite layers show larger distortion and dispersion in bond lengths compared those closer to outside of layers (**Table 3**). The local distortions around the cations and shift of the interstitial cations in such layered perovskites show lower symmetric structure and often a ferroelectric structure, which is explained later in this manuscript.

In order to further ascertain the structure and phase transformation in PTO, total energy calculation in DFT formalism were carried out. The calculated total energy and unit cell parameters of PTO in all the possible symmetry models are included in **Table 1**. The details of calculated structural parameters for $P2_1$ symmetry are included in **Table 2** and those for other symmetry models are provided as supplementary data (***Supplementary data S-II***) to this manuscript. It is observed that the PTO has almost equivalent energy in the $P2_1$ and $Pna2_1$ symmetry, while those for the ferroelectric $Cmc2_1$ and other paraelectric ($P2_1/m$ and Cmcm) model structures have higher values (about 0.05eV/atom). Thus the later models are not energetically favorable for the structure of PTO. From the comparison of energies, it can be suggested that the $P2_1$ or $Pna2_1$ ferroelectric structures can be retained at ambient temperature. It can be mentioned here that the structure in $Pna2_1$ and $P2_1$ symmetries are closely related. Typical unit cell relations between the orthorhombic $Pna2_1$ and monoclinic $P2_1$ structures are depicted in the **Figure 4**. The transformation from $Pna2_1$ to $P2_1$ symmetry is resulted from the shift of the Pr atoms and octahedral slabs along the c-axis, which destroy two of the glide planes of the former. As mentioned earlier the $Pna2_1$ symmetry cannot account for the weak reflections at $2\theta \sim 14.5°$. Also, the absence of measureable intensity at $2\theta \sim 12.4$ and 23.5° in the observed XRD data support for monoclinic $P2_1$ structure over the orthorhombic $Pna2_1$ for PTO. Further the variations of energies with volume for all the five relaxed structures were calculated and they are given as supplementary data (***Supplementary data SI-III***). In a wider range of volume, the variation of energy show almost similar trend for all except the $Cmc2_1$ structure. Similar to the fully relaxed states, the $Pna2_1$ and $P2_1$ structures do not show any difference with the change in volume. Almost identical energies for monoclinic ($P2_1$) and orthorhombic ($Pna2_1$) can be due to the calculations are made by DFT are at 0 K, without including the entropy contribution. The differences in the contributions of entropy at finite temperature may favor the monoclinic ($P2_1$) structure compared to the orthorhombic ($Pna2_1$) structure. At larger volume (above the molar volume (V_m) 152 $Å^3$), the orthorhombic $Cmc2_1$ structure is favored over orthorhombic $Pna2_1$ and monoclinic $P2_1$ structures.

In order to understand the electronic properties of PTO, the electron density of states (DOS) for all the relaxed structures were calculated. The total electronic density of states and the Pr, Ti, and O contributions (projected within their atomic spheres) are shown in **Figure 5**. From the calculated DOS, it is inferred that the lower lying states below -10 eV originate mainly from

O 2s and Pr n*p* orbitals. The states in the valence band region from -5 to 0 eV are mainly composed of O 2*p* orbitals which is hybridized with Ti 3*d* orbitals. This suggests the nature of the Ti–O bonding is largely covalent. Further, the states in the conduction band region from 2 to 6 eV have a dominant contribution from Ti 3*d* orbitals. The O 2*p* orbitals also contribute a little to the conduction band and hybridized to a small extent with Ti 3*d* orbitals. . The band gaps for the ferroelectric structures, like $P2_1$, $Pna2_1$ and $Cmc2_1$ structures are almost similar and are close to 2.7 eV, while those for the paraelectric phases, like $P2_1/m$ and Cmcm structures are low (~ 2.0 eV). This suggests the ferroelectric to paraelectric phase transition would decrease the band gap. The experimental optical band gap of PTO as observed from the absorption spectra (***Supplementary data SI-IV***) is 3.10 eV, which is in agreement with earlier reported value. [11] As commonly observed the band gap calculated by DFT is often underestimated compared to the true experimental gap. [41] This difference can be attributed to the limitation of the Kohn-Sham formalism to account the discontinuity of the exchange–correlation function.

The thermal properties like phase transition and stability of $Pr_2Ti_2O_7$ were investigated by thermogravimetric and differential thermal analyses (TG-DTA) in oxygen as well as in inert atmosphere. Typical TG-DTA traces recorded while heating the sample from ambient to 1673 K in oxygen or argon atmosphere are shown in **Figure 6**. No weight gain except the apparent baseline shift as seen from the TG traces recorded under argon or oxygen atmosphere suggests the retention of the 3+ state of praseodymium till the highest temperature. The DTA traces in both argon or oxygen atmosphere show deviations around 900°C and then a sharp deviation above around 1300°C. The TG residues obtained indicate no signature of melting of the sample. Shcherbakova et al. [3] have compiled the melting temperature for various rare-earth titanates and mentioned the melting temperature of $Pr_2Ti_2O_7$ is 1560°C. Thus, this deviation cannot be attributed to the melting point. The sharp endothermic peak above 1300°C coincides with the reported ferroelectric to paraelectric transition of PTO. [7] Yan et al. [4] have investigated analogous titanates, namely, $La_2Ti_2O_7$ and $Nd_2Ti_2O_7$ and observed the ferroelectric to paraelectric transitions are at 1482°C and 1461°C, respectively. Thus, the ferroelectric to paraelectric transition of $Pr_2Ti_2O_7$ though cannot be ruled out at 1300°C but more expected above 1400°C only. It can also be mentioned that at higher temperature, Ti^{4+} has a tendency to reduce to Ti^{3+} leaving oxygen vacancy. A feeble deviation in the TG traces at the corresponding temperatures of deviations in the DTA traces may be a support for this.

The XRD patterns of the residue obtained after TG-DTA runs indicate the presence of the original monoclinic $P2_1$ structure (**Figure 7)**. However, several extra reflections attributable to Ti rich perovskite type phase, ($Pr_2Ti_3O_9$) are observed in both the XRD patterns. This suggests a partial decomposition of the $Pr_2Ti_2O_7$ composition at higher temperature. The Rietveld refinements of the powder XRD patterns of the samples obtained after TG runs suggest no significant change in the unit cell or structural parameters of PTO lattice compared to the original ambient temperature phases. Gao et al. [7] and Sun et al. [17] have observed a dielectric anomaly at lower temperature, viz. below 800 K, which the authors have attributed to the ferroelectric to paraelectric phase transition. The lowering of the ferroelectric Tc, has been attributed to the preparation procedure and/or nanocrystalline nature of the sample. [4,7,17] Such anomaly is also seen in the present study on the dielectric and electrical properties. However, differential scanning calorimetric (DSC) investigation on PTO also did not show any anomaly attributable to phase transition up to 873 K (***Supplementary data S-IV***). The deviation in the DTA pattern above 1073 K observed in DTA traces recorded both in oxygen or argon atmosphere plausibly can be attributed for this affect. However no structural changes are noticed in both *in situ* high temperature XRD and Raman spectroscopic investigations of the present study. This indicates either absence of any structural transition or a transition accompanied by a very low energy change. Considering, the high temperature structural studies, it is concluded that the deviation in DTA traces are not related to the structural transition accompanied with ferroelectric to paraelectric phase transition. The details of high temperature behavior of the PTO, as observed by *in situ* variable temperature powder XRD studies are explained below.

Powder XRD patterns of PTO recorded at successive temperatures between ambient to 1273 K are shown in **Figure 8**. The XRD patterns recorded at higher temperature are almost similar to that observed at ambient temperature except the shift in positions due to thermal effect. Considering the refined structural parameters observed at ambient temperature, the XRD data recorded at different temperatures were refined by Rietveld refinement method. The refined unit cell parameters observed for ambient temperature phases are comparable to those observed in the ambient temperature data recorded on high temperature stage. The observed unit cell parameters at different temperature are given in **Table 4**. A comparison of the variations of unit cell parameters observed at different temperatures indicates a smooth variation with temperature. In order to see the possible phase transition, the XRD data recorded at and beyond 873 K were

analyzed by considering the possible symmetries of paraelectric ($P2_1/m$; Cmcm) and ferroelectric ($Cmc2_1$) phases. However, the observed peaks, in particular the differentiating peak at two-theta ~ 37.5°, could not be accounted by these models. Typical Rietveld refinement plot of the powder XRD data recorded at 1273 K is shown in **Figure 9**. Similar features are also observed in the XRD pattern of PTO recorded at 1473 K (shown as ***supplementary data SI-VI***), which suggests that PTO does not have any structural transition up to 1473 K. However, as observed from the variation of energy versus volume (***Supplementary data*** **SI-III**) the orthorhombic ($Cmc2_1$) structure has higher stability over the monoclinic ($P2_1$) or orthorhombic ($Pna2_1$) structures above the molar volume (V_m) 152 $Å^3$. From the high temperature XRD studies, it is observed that the unit cell volume at 1473K is 565.69(3) $Å^3$, i.e. V_m = 141.4 $Å^3$. Considering the average volume thermal expansion coefficient (between RT-1473K) as 32.3 x 10^{-6} K^{-1}, the expected unit cell volume of monoclinic ($P2_1$) at 1673 K is only about 569.2 $Å^3$ (V_m = 142.3 $Å^3$). Thus a phase transition from monoclinic ferroelectric ($P2_1$) to orthorhombic ($Cmc2_1$) can only be expected at still higher temperature. Hence it can be mentioned here that the ferroelectric to paraelectric phase transition is above 1473 K, as observed in other analogous titanates. [3,4,14]

Earlier studies on isostructural compound $La_2Ti_2O_7$ indicated a structural transition from ferroelectric ($P2_1$) to another ferroelectric ($Cmc2_1$) transition in between 993 to 1053 K, [24] which is similar to that reported for $Ca_2Nb_2O_7$. [42] In a recent study, Hererra et al. have reported both $P2_1$ and $Cmc2_1$ structures of $La_2Ti_2O_7$ at ambient temperature, in the sample prepared from xerogel method by heating at 1073 and 1273 K, respectively. [43] However, the reported XRD pattern indicated poorly crystalline nature of the phase where the differentiation of these two symmetries is not easy. In the present study and earlier studies on $La_2Ti_2O_7$ and related materials prepared by high temperature reactions show only $P2_1$ structure at ambient temperature. [18,20,24,25] Since the differentiation of these probable symmetries is difficult as they are mainly based on the presence or absence of weak reflections, the claim for the stabilization of $Cmc2_1$, which is also energetically unfavorable compared to $Pna2_1$ or $P2_1$ structures, cannot be relied. Thus we suggest no structural transition in PTO up to 1473 K.

Further to confirm the high temperature behavior of PTO, *in situ* high temperature Raman spectroscopic investigations were carried out. Raman modes being sensitive to the variation of

local coordination and distortion as well as to symmetry, the analyses of temperature dependent Raman mode can provide clear information on these features. At ambient conditions, $Pr_2Ti_2O_7$ has monoclinic structure with space group $P2_1$ (*point group: C_2)* and four formula units per unit cell which gives 132 normal modes of vibration. Factor group analysis gives irreducible mechanical representations for optic and acoustic modes as Γ_{optic} = 65A+64B and $\Gamma_{acoustic}$ = A+2B, respectively. From group theoretical calculations, 129 Raman active modes are expected in $Pr_2Ti_2O_7$. Earlier report suggested the presence of photoluminescence lines in $Pr_2Ti_2O_7$.[44] Hence to verify this; Raman spectra of $Pr_2Ti_2O_7$ using different laser excitation wavelengths at ambient conditions were recorded and they are given as supplementary data to this manuscript (***Supplementary data SI-VII***). It is observed that the excitation wavelengths, 532, 514 and 785 nm give identical spectra, while the excitation wavelengths lower than 488 nm show dominating luminescence in the Raman spectra. This indicates that all the peaks in the spectra with 532nm are Raman modes. All the spectra were recorded with excitation wavelength of 532 and they are presented in this manuscript. **Figure 10** shows the Raman spectra of PTO at different temperatures in between 298-1073 K. At ambient temperature 32 distinct Raman modes could be clearly identified. The less number of observed Raman modes than expected may be due to the degeneracy or weak nature of some modes. Low frequency modes in the range 50-490 cm^{-1} are attributed to the Pr-O vibrations. [16] Modes in the range 490-575 cm^{-1} are assigned to the vibrations of distorted TiO_6 octahedron. [16] The modes above 600 cm^{-1}, particularly the high frequency modes at 785 and 814 cm^{-1} are assigned to stretching modes of Ti-O vibrations. These stretching modes are separated from the rest mode with a gap. This feature is similar to the gap in between the stretching and bending vibrations of VO_4 tetrahedra in ABO_4 type orthovanadates. [45] Since the TiO_6 octahedra are distorted and bond strength of Ti-O are weaker compared to V-O bonds of VO_4 tetrahedra of orthovanadates, the gap between the bending and stretching modes are less in $Pr_2Ti_2O_7$ compared to that observed in orthovanadates.

The evolution of Raman modes with temperature were followed by comparing with the modes observed at ambient temperature. The temperature dependencies of Raman mode frequencies of PTO are shown in **Figure-11**. All the Raman modes broaden gradually with increase in temperature, due to which most of the weak intensity modes are not seen at higher temperatures. It is also observed that several weak modes could not be followed at higher temperatures due to overlapping caused by temperature induced broadening. From the variations

of mode frequency with temperature, it can be seen that almost all the modes soften with increasing temperature. Table 5 shows the temperature coefficients of Raman mode frequencies of PTO. Most of the Raman mode frequencies show linearly decreasing trend in the range 298-1073 K, which indicates that the anharmonicity in PTO is predominantly due to three phonon decay process. However, typical trend for some of the modes show anomalous behaviour. The modes at 217 and 814 cm^{-1} show negligible change in frequency in the temperature range. The lattice mode at 158 cm^{-1}, the mode at 312 cm^{-1}, which has been attributed to the Pr-O vibration and the mode at 785 cm^{-1} due to Ti-O stretching vibrations show increase in frequency with temperature. Generally, higher order terms of phonon-phonon interactions are responsible for such kind of anomaly. This anomalous behaviour could also be associated with symmetrization of the distorted PrO_n and TiO_6 polyhedra. At higher temperature, it is possible that phonon anomaly could bring instability in the structure, which could lead to ferroelectric to paraelectric phase transition. The smooth variation of Raman modes within temperature range 298-1073 K suggests absence of any structural transition. Thus the Raman spectroscopic studies do not show any signatures of phase transition in the temperature range studied; but the possibility of ferroelectric to paraelectric phase transition at higher temperature cannot be ruled out.

Microstructural features of sintered PTO samples were investigated by scanning electron microscopy. The SEM pictures of the top and fractured surfaces of the prepared pellets are given as supplementary data (***Supplementary data S-VII***) to this manuscript. Irregular micron sized well connected grains are observed under the preparation condition. However, the observed grains are quite different in shape and connections from the samples prepared from the low temperature solution processing and spark plasma sintered samples. [4,7] However, in the present case no such preferred orientation or well developed facets are observed under the employed sintering condition. At higher sintering temperature, such layered materials can exhibit highly oriented grain growth as seen by Gao et al. [7] The differences might be attributed to the differences in the sintering temperature. Since a partial decomposition at higher temperature is observed in this study, further high temperature processing was not been carried out. Besides, at higher temperature differences in the composition and oxidation state of cations may also occur in PTO.

The measurement of electric polarization (P) with applied potential (E) at ambient temperature show typical ferroelectric like loops and is in agreement with the ferroelectric nature of PTO. Typical PE loop of PTO is shown in **Figure 12**. No saturation of polarization is observed up to the maximum applied voltage of this study. This might be due to higher loss arising from low density of the studied pellets. The observed maximum polarization (Ps), remanent polarization (P_r) and coercive field (E_c) are 0.017 μC/cm^2, 0.005 μC/cm^2 and 235 V, respectively. Typical loss current of about 0.1 μamp is observed at 1200 V.

Further to understand the ferroelectric to paraelectric phase transition, the refined structural models are compared. All the structures can be compared by using unit cell and symmetry relations are as shown in **Figure 1**. It can be mentioned here that the paraelectric $P2_1/m$ or Cmcm structures differ from the parent ferroelectric $P2_1$ structure in both octahedral distortion as well as displacement of the metal ion positions. Recently, the density functional calculations on a similar layered perovskite $La_2Ti_2O_7$ and $Nd_2Ti_2O_7$ indicated a similar energy variation between different symmetries and the authors concluded that the transformation from monoclinic $P2_1$ to Cmcm may occur through an intermediate $P2_1/m$ phase. [14] The total energy calculations of this study also support for a similar transformation sequence. Similar studies on the ferroelectric transition by Perez-Lopez et al. [15] suggested the shift of the position of rare-earth and the rotation of TiO_6 octahedral units are linked to the transition. From the energy variations, it can be suggested that the structure may transform to another ferroelectric $Cmc2_1$ phase before transformation to paraelectric phases. But in the present *in situ* high temperature XRD and Raman spectroscopic investigations indicate no distinct phase transition in PTO.

In order to compare the ferroelectric and paraelectric phase of PTO, it is ideal to compare the structure with $P2_1/m$ and $P2_1$ symmetries due to the simple symmetrically related displacive and strain free nature of lattice transformation. The two structures in the unit cell of $P2_1$ and the polarization arising from the ionic displacements along the polar axis, *i.e.* b-axis, are shown in **Figure 13.** The spontaneous polarization as calculated from the shift of the ions in the b-axis is 8.3 μC/cm^2. The calculated polarization of PTO is comparable to that reported for $La_2Ti_2O_7$ (7.4-7.7 μC/cm^2). [14,15] It can be mentioned here the electric polarization observed for $La_2Ti_2O_7$ and $Nd_2Ti_2O_7$ are in the range of 5 to 9 μC/cm^2 [4,46] while that of $Pr_2Ti_2O_7$ thin films is about 1-

4 μC/cm^2. [17,47] The lower observed experimental values might be due to relatively higher conducting contribution as well as polycrystalline nature of the sample in present study.

Additional electrical properties of PTO were studied by the impedance spectroscopic investigation. The temperature dependent permittivity and loss spectra in between 173 to 473 K are shown in **Figure 14**. In the studied frequency range, both the spectra indicate two different types of dielectric responses. The low frequency relaxations show significant temperature dependence, with the loss peak moving towards higher frequencies as the temperature rises, whereas the high frequency relaxation is almost invariant with temperature. The permittivity spectra recorded up to 473 K show almost similar behavior. However, at still higher temperature the permittivity shows sharp rise at lower frequency compared to that at higher frequency. A comparison of the temperature dependent permittivity and loss features suggests that at higher temperature an appreciable ion migration causes interfacial polarization leading to sharp rise in permittivity due to the Maxwell Wagner (MW) effect.

The frequency-dependent complex permittivity $\varepsilon^*(\omega)$ can be most generally represented by the Havriliak-Negami (H-N) model as given below [48]

$$\varepsilon^*(\omega) = \varepsilon_\infty + (\varepsilon_s - \varepsilon_\infty)/[1 + (i\omega\tau)^\alpha]^\beta \quad (1)$$

where $\omega = 2\pi f$ is the angular frequency, τ is the relaxation time, ε_s and ε_∞ are the low and high frequency values of permittivity, respectively, $i = \sqrt{-1}$, and α and β are exponents such that $\alpha > 0$, $\alpha\beta \leq 1$. The contribution due to electrical conductivity can be incorporated by adding the term $(-i[\sigma_{dc}/(\varepsilon_0\omega)]^n)$ to Eq. (1), where σ_{dc} is the *dc*-conductivity, ε_0 is the permittivity of free space, and $n \approx 1$.

We have further analyzed these two dielectric responses by fitting two H-N relaxation models and a conductivity contribution to the measured dielectric loss spectra as below

$$\varepsilon^*(\omega) = \varepsilon_\infty + \frac{\varepsilon_s - \varepsilon_\infty}{[1 + (i\omega\tau_1)^{\alpha_1}]^{\beta_1}} + \frac{\varepsilon_s - \varepsilon_\infty}{[1 + (i\omega\tau_2)^{\alpha_2}]^{\beta_2}} - i[\sigma_{dc}/(\varepsilon_0\omega)]^n \quad (2)$$

where the subscripts 1 and 2 corresponds to the low and high frequency relaxations, respectively. Typical fit of the $\varepsilon''(\omega)$ Havriliak-Negami (H-N) model is shown as supplementary data to this manuscript (***Supplementary data S-IX***).

The relaxation time τ_1 extracted from this fitting was found to follow the Arrhenius relation (Eq. 3) which suggest the relaxation is a thermally activated process

$$\tau_1 = \tau_0 \exp(E_1 / k_B T) \quad (3)$$

where τ_0 is a pre-exponential factor, E_1 is the activation energy, and T is the temperature of measurement. The typical Arrhenius plot of the relaxation time τ_1 is depicted in **Figure 15**. In contrast to τ_1, the relaxation time τ_2 for the second (high frequency) process does not show any significant variation with temperature (see inset in **Figure 15**). Thus, the first relaxation is a thermally activated process, and can be attributed to the Maxwell-Wagner polarization arising from the grain boundaries. This was further confirmed by the decrease in the dielectric strength (ε_s-ε_∞) with temperature (**Figure 16)**. Similar to the relaxation time, the behavior of the dielectric strength for the second relaxation is also quite different (**Figure 16)**, and thus we conclude this relaxation is not of the Maxwell-Wagner type**.** Thus this relaxation can be attributed to the dipolar origins and is related to the realignment of the dipoles with the oscillation of applied electric field. The Maxwell-Wagner relaxations due to grain boundaries are essentially a low frequency phenomenon, since the interfacial polarization cannot follow the applied *ac*-field of higher frequencies, and thus the dielectric strength diminishes with temperature. [49] The value of permittivity (dielectric constant) measured in our study is around 18 at 10 kHz and remains almost unchanged with temperature. This value is somewhat lower than that observed for $Pr_2Ti_2O_7$ by Gao et al. [7] but close to that obtained by Sun et al. [17] for nanocrystalline $Pr_2Ti_2O_7$. The low values of loss tangent, viz. 0.2-0.3 at 10 kHz, indicate the low loss characters of PTO.

To follow the dielectric properties at still higher temperature, the impedance spectroscopic studies at higher temperature were carried out. The variation of permittivity and *tanδ* with temperature are shown in **Figure 17**. The temperature dependent permittivity shows a peak like feature around 673 K, which is similar to the ferroelectric like transition observed by Sun et al. [17] Despite the crystalline nature of the present studied sample, this anomaly coincides with results of Sun et al. [17] A gradually decreasing trend of permittivity and shifting of peak

temperature towards higher temperature are observed with increasing frequency. The variation of peak temperature with frequency follows Arrhenius relation and thus again support for a thermal activated process in PTO. At lower frequencies, sharp rise in permittivity is observed. Such behaviours are expected for ionic conductor due to polarization of electrodes. This indicates that the low frequency dielectric anomaly is not related to the polar orientation. A sharp increase in loss tangent at higher temperature is observed in the variation of *tanδ* with temperature. Though the values of loss tangent are small at lower temperature, they show considerably larger values at higher temperature. Thus at higher temperature, PTO shows appreciable ionic conduction which can be either due to the formation of intrinsic defects or annihilation of defect clusters. Thus the dielectric anomaly is related to ionic movement in the system. In order to understand the electrical conductivity the total conductivity were extracted from the impedance data and the temperature dependent conductivities are shown in **Figure 18**. From the **Figure 18**, it is observed that the conductivity decreases appreciably below 873 K. The activation energy for conductivity as obtained from Arrhenius relation is 0.60 eV. The observed activation energy is more similar for a mixed ionic conductor as observed earlier in $Pr_2Zr_2O_7$ and other related systems. [50,51] It can be mentioned here even though $Pr_2Ti_2O_7$ and $Pr_2Zr_2O_7$ have different crystal structure, the activation energies for electrical conductivities are not significantly different, viz. $Pr_2Ti_2O_7$ (0.60 eV) and $Pr_2Zr_2O_7$ (0.42 eV). [50] In both case the mixed electronic conductivities are expected from the variation of oxidation state of Pr, due to partial oxidation of Pr^{3+} to Pr^{4+}. However, $Pr_2Zr_2O_7$ show significant oxidation of Pr^{3+} to Pr^{4+} at higher temperature in air due to more open nature of pyrochlore structure compared to the perovskite structure of $Pr_2Ti_2O_7$. Also the inter-cation (Pr^{3+}-Pr^{3+}, electron hopping sites) distances are larger in $Pr_2Ti_2O_7$ compared to those in $Pr_2Zr_2O_7$. In addition appreciable amounts of interstitial oxygen ions in $Pr_2Zr_2O_{7+x}$ favor for oxide ion conduction in the lattice. Thus the observed activation energy of $Pr_2Ti_2O_7$ is little higher compared to $Pr_2Zr_2O_7$, but not appreciably different.

From the dielectric and impedance data it is observed that the electrical properties of $Pr_2Ti_2O_7$ are cumulative effects of the grain boundary and ionic and/or electronic defects. The dielectric behaviour is similar to any of the ferroelectric materials while at higher temperature the migration of ions, in particular anions and electrons due to the feeble valence fluctuation of Pr^{3+} may occur. The anionic defects can be easily formed in the perovskite sub-lattice, either during the preparation or due to a slight deviation in the composition. Since the ferroelectric properties

are related to the metal ion shifts and distortion of the TiO_6 octahedra, a feeble deviation in oxygen may not alter the polar character drastically, but at higher temperature they appear as loss contribution due to ion or electron movement.

4. CONCLUSIONS

From the ambient temperature XRD and Raman studies, a monoclinic $P2_1$ structure is established as the stable structure of $Pr_2Ti_2O_7$. The crystal structure is further supported from the *ab-initio* total energy calculations in DFT formalism. From the density functional calculations, it is observed that $Pna2_1$ and $P2_1$ have almost similar stability while the paraelectric $P2_1/m$ or Cmcm structures have least stability at ambient temperature. A partial decomposition at 1673 K is noticed in $Pr_2Ti_2O_7$. From the analyses of symmetry and structure, it was inferred that the ferroelectric ($P2_1$) to paraelectric ($P2_1/m$) is due to the displacement of cations along b-axis and rotation of TiO_6 octahedral units around the *a*-axis. No structural transition to $Cmc2_1$ from ambient to 1473 K was observed. From the volume dependent energy calculations and high temperature XRD studies, it is revealed that PTO may transform to another ferroelectric orthorhombic ($Cmc2_1$) structure at still higher temperature. The electron density of state calculations revealed that the ferroelectric $Pr_2Ti_2O_7$ has a band gap of ~ 2.7 eV which is close to the experimentally observed band gap of 3.10 eV. The measurement of field dependent electric polarization indicates the ferroelectric nature of PTO. The low temperature dielectric data indicate two different types of relaxations, one at lower frequency side due to thermally activated polarization process at the grain boundaries and other at higher frequency due to dipolar reorientation. The activation energy for thermally activated relaxation process is 0.38 eV and can be attributed interfacial polarization due to the ionic movements. At still higher temperature the dielectric properties are dominated by the ionic conduction.

ACKNOWLEDGMENT

The Department of Atomic Energy's Science Research Council (DAE-SRC) is acknowledged for supporting this work vide sanction number no. 2010/21/9-BRNS/2025 dated 7-12-2010.

Supporting Information

Rietveld refinement plots and structural parameters of $Pr_2Ti_2O_7$ in different model symmetry, Differential scanning calorimetric traces and scanning electron microscopic images of $Pr_2Ti_2O_7$ are supplied as Supporting Information.

References

(1) M. A. Subramanian, G. Aravamudan and G. V. Subba Rao, Prog. Solid State Chem., **15,** 55 (1983).

(2) A.W. Sleight, Inorg. Chem., **7**, 1704 (1968**).**

(3) L. G. Shcherbakova, L. G. Mamsurova and G. E. Sukhanova, Russ. Chem. Rev., **48**, 228 (1979).

(4) H. Yan, H. Ning, Y. Kan, P. Wang and M. Reece, J. Am. Ceram. Soc., **92**, 2270 (2009).

(5) T. –M. Pan, M. –D. Huang, C. –W. Lin, M. –H. Wu, Sensor and Actuat. B**, 144,** 139 (2010).

(6) S. Nanamatsu, M Kimura, K. Doi, S. Matsushita and N. Yamada, Ferroelectrics, **8**, 511 (1974).

(7) Z. P. Gao, H. X. Yan, H. P. Ning and M. J. Reece, Adv. Applied Ceramics, **112**, 69 (2013).

(8) M. Kimura, S. Nakamatsu, T. Kawamura and S. Matsushita, Jpn. J. Appl. Phys., **13**, 1473 (1974).

(9) N. A. Zakharov, V. S. Krikorov, E. F. Kustov and S. Y. Stefanovich, Phys. Status Solidi A, **50**, K13 (1978).

(10) N. A. Zakharov, S. Y. Stefanovich, E. F. Kustov and Y. N. Venevtsev, Krist. Tech., **15**, 29 (1980).

(11) D. W. Hwang, J. S. Lee, W. Li and S. H. Oh, J. Phys. Chem. B**, 107,** 4963 (2003).

(12) Z. Shao, S. Saitzek, P. Roussel, O. Mentre, F. P. Gheorghiu, L. Mitoseriu and R. Desfeux, J. Solid State Chem., **183**, 1652 (2010).

(13) C. Wenger, G. Lupina, M. Lukosius, O. Seifarth, H. -J. Mussig, S. Pasko and C. Lohe, J. Appl. Phys., **103**, 104103 (2008).

(14) E. Bruyer and A. Sayede, J. Appl. Phys., **108**, 053705 (2010).

(15) J. Lopez-Perez and J. Iniguez, Phys. Rev. B, **84,** 075121 (2011).

(16) V. V. Atuchin, T. A. Gavrilova, J. -C. Grivel, V. G. Kesler and I. B. Troitskaia, J. Solid State Chem., **195**, 125 (2012).

(17) L. Sun, L. Ju, H. Qin, M. Zhao, W. Su and J. Hu, Physica B, **431**, 49 (2013).

(18) P. M. Gasperin, Acta. Crvst. B, **31**, 2129 (1975).

(19) P. A. Kozmin, N. A. Zakharov and M. D. Surazhskaya, Inorganic Materials**, 33,** 850 (1997).

(20) N. Ishizawa, F. Maruo, S. Iwai, M. Kimura and T. Kawamura, Acta Cryst. B**, 36,** 763 (1980).

(21) K. Scheunemann and H. Mueller-Buschbaum, J. lnorg. Nucl. Chem., **36,** 1965 (1974).

(22) K. Scheunemann and H. Mueller-Buschbaum, J. Inorg. Nucl. Chem., **37**, 1879 (1975).

(23) E. J. Harvey, S. E. Ashbrook, G. R. Lumpkin and S. A. T. Redfern, J. Mater. Chem., **16**, 4665 (2006).

(24) N. Ishizawa, F. Marumo and S. I. Iwai, Acta Cryst. B**, 38,** 368 (1982).

(25) N. Ishizawa, K. Ninomiya, T. Sakakura and J. Wang, Acta. Cryst. E, **69**, i19 (2013).

(26) J. M. Pruneda and E. Artacho, Phy. Rev. B**, 72,** 085107 (2005).

(27) Z. L. Zhang, H. Y. Xiao, X. T. Zu, F. Gao and W. J. Weber, J. Mater. Res., **24**, 1335 (2009).

(28) H. Y. Xiao, L. M. Wang, X. T. Zu, J. Lian and R. C. Ewing, J. Phys.: Condens. Matter **19,** 346203 (2007).

(29) A. C. Larson and R. B. van Dreele GSAS: General Structure Analysis System. Los Alamos National Laboratory, Report LA-UR 86-748, 2000.

(30) Rodriguez-Carvajal, J. Fullprof 2000: A Program for Rietveld, Profile Matching and Integrated Intensity Refinements for X-ray and Neutron Data. Version 1.6, Laboratoire Leon Brillouin, Gif sur Yvette, France, **2000**.

(31) A. P. Roy, S. K. Deb, M. A. Rekha and A. K. Sinha, J. Pure Appl. Phys., **30**, 724 (1992).

(32) P. E. Blöchl, Phys. Rev. B**, 50,** 17953 (1994).

(33) P. Hohenberg and W. Kohn, Phys. Rev. B, **136**, 864 (1964).

(34) W. Kohn and L. J. Sham, Phys. Rev. A, **140**, 1133 (1965).

(35) G. Kresse and J. Furthmüller, Comput. Mater. Sci., **6**, 15 (1996).

(36) G. Kresse and D. Joubert, Phys. Rev. B, **59**, 1758 (1999**).**

(37) J. P. Perdew, K. Burke and M. Ernzerhof, Phys. Rev. Lett., **77**, 3865 (1996).

(38) J. P.Perdew, K. Burke and M. Ernzerhof, Phys. Rev. Lett.. **78,** 1396 (1997).

(39) H. J. Monkhorst and J. D. Pack, Phys. Rev. B**, 13,** 5188 (1976).

(40) R. L. C. Park, J. Am. Ceram. Soc., **78**, 3171 (1995).

(41) V. Panchal, D. Errandonea, A. Segura, P. Rodriguez-Hernandez, A. Muñoz A, S. Lopez-Moreno and M. Bettinelli, J. Appl. Phys., 110, 043723 (2011).

(42) J. K. Brandon and H. D. Megaw, Philos Mag., **21**, 189 (1970).

(43) G. Herreraa, J. Jiménez-Mierc and E. Chavira, Materials Characterization, **89**, 13 (2014).

(44) S. Saha, S. Prusty, S. Singh, R. Suryanarayanan, A. Revcolevschi and A. K. Sood, J. Solid State Chem., **184,** 2204 (2011).

(45) D. Errandonea, S. N. Achary, J. Pellicer-Porres and A. K. Tyagi, Inorg. Chem., **52**, 5464 (2013).

(46) W. S. Kim. S. -M. Ha, S. Yun and H. -H. Park, Thin Solid Films**, 420-421**, 575 (2002).

(47) A. Bayart, S. Saitzek, A. Ferri, R. Pouhet, M. –H. Chambrier, P. Roussel and R. Desfeuxa, Thin Solid Films**, 553,** 71 (2014).

(48) A. Schönhals and F.Kremer *Broadband Dielectric Spectroscopy*, edited by F. Kremer and A. Schönhals (Springer Verlag, Berlin, 2003).

(49) C. C. Wang, H. B. Lu, K. J. Jin and G. Z. Yang, Phys. Lett. B**, 22,** 1297 (2008).

(50) K. Vasundhara, S. N. Achary and A. K. Tyagi. Int. J. Hydrogen Energy, **40**, 4252 (2015).

(51) J. Zhang, W. Peng, Z. Chen, H. Chen and L. Han, J. Phys. Chem. C, **116**, 19182 (2012).

Tables

Table 1: Comparison of refined unit cell parameters and residuals of refinement in different structural models of $Pr_2Ti_2O_7$. Unit cell parameters and energy of different model as calculated by DFT are shown in italic font.

Table 2: Refined position coordinates of $Pr_2Ti_2O_7$ (at RT). The calculated positional parameters are shown below each parameter.

Table 3: Typical inter-atomic distances in structure of $Pr_2Ti_2O_7$.

Table 4: Refined unit cell parameters of $Pr_2Ti_2O_7$ at different temperatures.

Table 5: Temperature coefficients of Raman modes (ω) of $Pr_2Ti_2O_7$.

Figure Legends

Figure 1: Relations between different model structures of $Pr_2Ti_2O_7$.

Figure 2: Rietveld refinement plot of $Pr_2Ti_2O_7$ in $P2_1$ model.

Figure 3: Crystal structure of $Pr_2Ti_2O_7$in different projection (TiO_6octahedra are shown, isolated spheres are Pr atoms).

Figure 4: Comparison of monoclinic $P2_1$ and orthorhombic $Pna2_1$ structures of $Pr_2Ti_2O_7$. Only cations are shown (Larger sphere: Pr^{3+} and Small sphere: Ti^{4+}). The unit cell are related as: $a_o = 2c_m cos(\beta\text{-}90)$, $b_o = a_m$, $c_o = b_m$.

Figure-5. Calculated density of states of $Pr_2Ti_2O_7$ for different structures. (For $P2_1$, $Pna2_1$ and $Cmc2_1$ model, the band gaps are similar (~2.7 eV) while for the paraelectric Cmcm and $P2_1/m$, the band gaps have lower values (~ 2 eV).

Figure 6: TG/DTA curves of $Pr_2Ti_2O_7$ while heating from ambient to 1673K. (Heating rate = 10°C/min).

Figure 7: XRD patterns of $Pr_2Ti_2O_7$ recorded after heating at 1673K in argon and oxygen atmosphere

(Argon) : a = 7.7158(2) Å, b = 5.5878(2)Å, c = 13.0031(4) Å, β = 98.572(6)°, V = 544.43(2) $Å^3$. R_p = 9.78 %, R_{wp} = 12.9 % and χ^2 = 1.749

(Oxygen): a = 7.7159(2) Å, b = 5.5878(2) Å, c = 13.0021(3) Å, β = 98.582(4)°, V = 544.39(2) $Å^3$. Rp = 9.63 %, Rwp= 12.7 % and χ^2 = 1.884

Figure 8: Typical powder XRD patterns of PTO recorded at different temperatures.

Figure 9: Typical Rietveld refinement plot of XRD data of PTO recorded at 1273 K. (Lower vertical ticks indicate Bragg position (upper panel: $Pr_2Ti_2O_7$ and Lower panel: sample holder). (Rp = 15.7 %, Rwp = 20.8 %, $\chi 2$ = 1.67)

Figure 10: Raman spectra of $Pr_2Ti_2O_7$ at different temperatures.

Figure 11: Temperature dependence of Raman mode frequencies of $Pr_2Ti_2O_7$.

Figure 12: Ambient temperature PE loop of $Pr_2Ti_2O_7$.

Figure 13: Comparison of monoclinic ferroelectric $P2_1$ and paraelectric $P2_1/m$ structures of $Pr_2Ti_2O_7$. Light shades: $P2_1/m$ structure and colour: $P2_1$ structure. The spontaneous polarizations along b-axis due to shift of various ions are shown in right hand side figure.

Figure 14: Temperature dependent ε' (a and b) and ε'' (c and d) of $Pr_2Ti_2O_7$in low temperature region.

Figure 15: Typical Arrhenius fit for low temperature relaxation (τ_1) of $Pr_2Ti_2O_7$. The temperature dependency of τ_2 is shown as inset.

Figure 16: Variation of dielectric strength of the two low temperature relaxations of $Pr_2Ti_2O_7$ with temperature.

Figure 17: Temperature dependent ε' and *tanδ* of $Pr_2Ti_2O_7$ at selected frequencies in high temperature region.

Figure 18: Variation of total conductivity of $Pr_2Ti_2O_7$with temperature at high temperature (Arrhenius fits are shown as solid line).

Table 1: Comparison of refined unit cell parameters and residuals of refinement in different structural models of $Pr_2Ti_2O_7$. Unit cell parameters and energy of different model as calculated by DFT are shown in italic font.

	$P2_1$ (No. 4)	$Pna2_1$ (No. 33)	$Cmc2_1$ (No. 36)	$P2_1/m$ (No. 11)	Cmcm (No. 63)
a (Å)	7.7152(1)	25.7197(4)	3.8575(1)	7.7146(2)	3.8573(1)
b (Å)	5.4878(1)	7.7151(1)	25.7194(5)	5.4874(1)	25.7197(6)
c (Å)	13.0042(2)	5.4877(1)	5.4877(1)	13.0036(4)	5.4872(1)
β (°)	98.552(4)			98.531(7)	
V	544.47(2)	1088.92(3)	544.46(2)	544.40(3)	544.38(2)
Z	4	8	4	4	4
ρ	5.973g/cc	5.973g/cc	5.973g/cc	5.974g/cc	5.974g/cc
R_p	0.0616	0.0804	0.0834	0.1192	0.1066
R_{wp}	0.0775	0.1001	0.1084	0.1496	0.1433
χ^2	3.758	5.899	6.791	10.64	10.72
RF^2	0.0630	0.0892	0.1008	0.1856	0.1603
a	*7.7540*	*26.3100*	*3.8502*	*7.8665*	*3.92706*
b	*5.5610*	*7.7550*	*25.6992*	*5.5450*	*26.39951*
c	*13.3010*	*5.5600*	*5.7720*	*13.3455*	*5.54500*
β (°)	*98.436*			*98.529*	
E/atom (eV)	*-8.6630*	*-8.6630*	*-8.6526*	*-8.6166*	*-8.6009*

Table 2: Refined position coordinates of $Pr_2Ti_2O_7$ (at RT). The calculated positional parameters are shown below each parameter.

Atoms	*Wyc.*	x	y	z	100× Uiso(Å)^2
Pr1	*2a*	0.2841(8)	0.2539(24)	0.11325(20)	2.21(7)
		0.2815	0.2536	0.1218	
Pr2	*2a*	0.7763(9)	0.2559(6)	0.09940(21)	2.49(7)
		0.7706	0.2651	0.0887	
Pr3	*2a*	0.3557(9)	0.7988(5)	0.39211(21)	3.22(8)
		0.3506	0.7958	0.3813	
Pr4	*2a*	0.8526(9)	0.8421(5)	0.41616(22)	3.46(9)
		0.8543	0.8666	0.4288	
Ti1	*2a*	0.0370(10)	0.7619(7)	0.1215(4)	0.71(19)
		0.0315	0.7699	0.1198	
Ti2	*2a*	0.5455(9)	0.7682(7)	0.1200(4)	0.37(18)
		0.5282	0.7680	0.1222	
Ti3	*2a*	0.0724(10)	0.2972(8)	0.3247(4)	1.63(25)
		0.0719	0.2970	0.3199	
Ti4	*2a*	0.5668(9)	0.2934(7)	0.3226(4)	0.33(20)
		0.5847	0.3043	0.3253	
O1	*2a*	0.7859(10)	0.8481(10)	0.1082(16)	2.58(17)
		0.7774	0.8209	0.1097	
O2	*2a*	0.2886(10)	0.7248(10)	0.0969(15)	2.58(17)
		0.2729	0.6774	0.0921	
O3	*2a*	0.0279(50)	0.0213(9)	0.0160(8)	2.58(17)
		0.0439	0.0251	0.0199	
O4	*2a*	0.4802(46)	0.0578(9)	0.0302(7)	2.58(17)
		0.4667	0.0243	0.0217	
O5	*2a*	0.0151(35)	0.9512(9)	0.2357(8)	2.58(17)
		0.1171	0.9647	0.2280	
O6	*2a*	0.4881(26)	0.9621(9)	0.2235(8)	2.58(17)
		0.4967	0.9610	0.2307	
O7	*2a*	0.0447(65)	0.4576(9)	0.1842(8)	2.58(17)
		0.0223	0.4512	0.1828	
O8	*2a*	0.5776(46)	0.4591(9)	0.1822(8)	2.58(17)
		0.5674	0.4476	0.1810	
O9	*2a*	0.0734(50)	0.5244(10)	0.4222(10)	2.58(17)
		0.0781	0.5646	0.4057	
O10	*2a*	0.6232(51)	0.5605(9)	0.4002(13)	2.58(17)
		0.6266	0.5894	0.3878	
O11	*2a*	0.1533(40)	0.0521(9)	0.4200(12)	2.58(17)
		0.1304	0.0780	0.4284	
O12	*2a*	0.5954(59)	0.0635(9)	0.4263(10)	2.58(17)
		0.5901	0.0970	0.4407	
O13	*2a*	0.3230(11)	0.3908(10)	0.3168(16)	2.58(17)
		0.3273	0.3607	0.3060	
O14	*2a*	0.8181(10)	0.2440(10)	0.3124(15)	2.58(17)
		0.8261	0.2042	0.3055	

Space Group: $P2_1$ (No. 4), Z = 4(Rp: 6.16, Rwp: 7.75, $\chi 2$ = 3.76; $R_{(F2)}$ = 6.29
a : 7.7152(1), b = 5.4878(1), c = 13.0042(2) Å, β = 98.552(4), V = 544.47(1) Å^3
*a = 7.7540, b = 5.5610, c = 13.3010*Å, *β = 98.47° (DFT results)*

Table 3: Typical inter-atomic distances in structure of $Pr_2Ti_2O_7$.

Bonds	Dist. (Å)	Bonds	Dist. (Å)	Bonds	Dist. (Å)	Bonds	Dist. (Å)
Pr1_O1	2.896(20)	Pr3_O6	2.705(13)	Ti1_O1	1.976(9)	Ti3_O5	2.233(8)
Pr1_O2	2.912(15)	Pr3_O9	2.723(32)	Ti1_O2	2.024(10)	Ti3_O7	2.010(9)
Pr1_O2	2.594(15)	Pr3_O10	2.433(34)	Ti1_O3	1.971(8)	Ti3_O9	1.777(10)
Pr1_O3	2.528(29)	Pr3_O10	3.041(16)	Ti1_O3	2.220(9)	Ti3_O11	1.872(11)
Pr1_O3	3.093(28)	Pr3_O11	2.161(25)	Ti1_O5	1.840(10)	Ti3_O13	2.018(10)
Pr1_O4	2.258(28)	Pr3_O12	2.341(35)	Ti1_O7	1.856(7)	Ti3_O14	1.966(9)
Pr1_O6	2.535(16)	Pr3_O12	2.668(12)				
Pr1_O7	2.45(4)	Pr3_O13	2.442(10)				
Pr1_O8	2.568(31)						
Pr1_O13	2.724(20)	Pr3_O10	3.187(24)				
			8				
CN	10	CN	8	CN	6	CN	6
BVS	2.98(9)	BVS	3.00(1)	BVS	4.04(5)	BVS	4.12(5)
Distt	79.80×10^{-4}	Distt	100.62×10^{-4}	Distt	40.39×10^{-4}	Distt	47.50×10^{-4}

Bonds	Dist. (Å)	Bonds	Dist. (Å)	Bonds	Dist. (Å)	Bonds	Dist. (Å)
Pr2_O1	2.241(6)	Pr4_O5	2.883(17)	Ti2_O1	1.934(10)	Ti4_O6	2.259(8)
Pr2_O2	2.533(20)	Pr4_O9	2.431(27)	Ti2_O2	1.975(9)	Ti4_O8	2.053(10)
Pr2_O3	2.688(32)	Pr4_O9	2.322(13)	Ti2_O4	1.992(9)	Ti4_O10	1.796(10)
Pr2_O3	2.707(27)	Pr4_O10	2.336(30)	Ti2_O4	2.252(9)	Ti4_O12	1.836(10)
Pr2_O4	2.569(30)	Pr4_O11	2.584(29)	Ti2_O6	1.822(10)	Ti4_O13	1.946(9)
Pr2_O4	2.917(22)	Pr4_O11	2.666(15)	Ti2_O8	1.880(7)	Ti4_O14	1.982(10)
Pr2_O5	2.891(17)	Pr4_O12	2.35(4)				
Pr2_O7	2.46(4)	Pr4_O14	2.579(11)				
Pr2_O8	2.290(27)						
Pr2_O14	2.741(19)						
CN	10	CN	8	CN	6	CN	6
BVS	3.38	BVS	2.98(9)	BVS	4.12(6)	BVS	4.17(6)
Distt	69.99×10^{-4}	Distt	79.80×10^{-4}	Distt	50.82×10^{-4}	Distt	59.18×10^{-4}

Table 4: Refined unit cell parameters of $Pr_2Ti_2O_7$ at different temperatures.

Temp (K)	a (Å)	b (Å)	c (Å)	β (°)	V (Å)^3
300	7.7184(4)	5.4898(3)	13.0076(9)	98.59(2)	544.98(6)
473	7.7336(3)	5.5003(2)	13.0224(7)	98.57(2)	547.75(4)
673	7.7518(3)	5.5135(2)	13.0423(7)	98.56(2)	551.21(4)
873	7.7683(3)	5.5246(2)	13.0613(7)	98.59(1)	554.26(4)
1073	7.7882(3)	5.5387(2)	13.0833(7)	98.58(1)	558.05(4)
1273	7.8107(3)	5.5543(2)	13.1080(6)	98.59(1)	562.28(4)
1473	7.8264(2)	5.5658(1)	13.1338(4)	98.60(1)	565.69(3)

Table 5 Temperature coefficients of Raman modes (ω) of $Pr_2Ti_2O_7$.

Mode ω (cm^{-1})	dω/dT (cm^{-1}/K)	Mode ω (cm^{-1})	dω/dT (cm^{-1}/K)
59	-0.007	269	-0.012(1)
72	-0.009	284	-0.020(1)
80	-0.004(1)	312	0.006(2)
91	-0.009(1)	327	-0.010(4)
105	-0.010	350	-0.015(1)
115	-0.013	385	-0.022(1)
136	-0.010(1)	431	-0.017(1)
158	0.003	453	-0.005(1)
172	-0.019(2)	487	-0.003(2)
179	-0.004(1)	504	-0.003(1)
193	-0.019(2)	526	-0.018(2)
200	-0.027(4)	540	-0.023(2)
217	0	565	-0.034(3)
231	-0.010(1)	605	-0.031(1)
249	-0.012(1)	785	0.003(1)
261	-0.014(1)	814	0

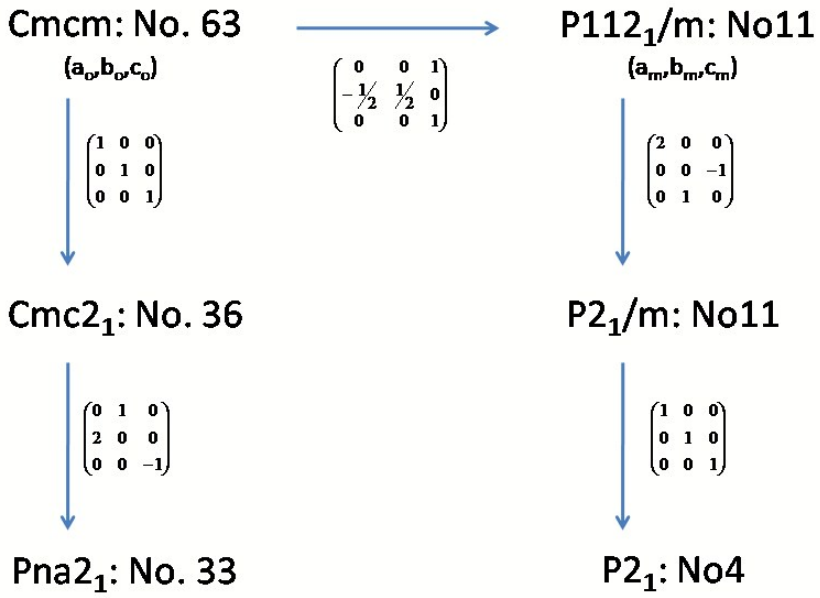

Figure 1: Relations between different model structures of $Pr_2Ti_2O_7$.

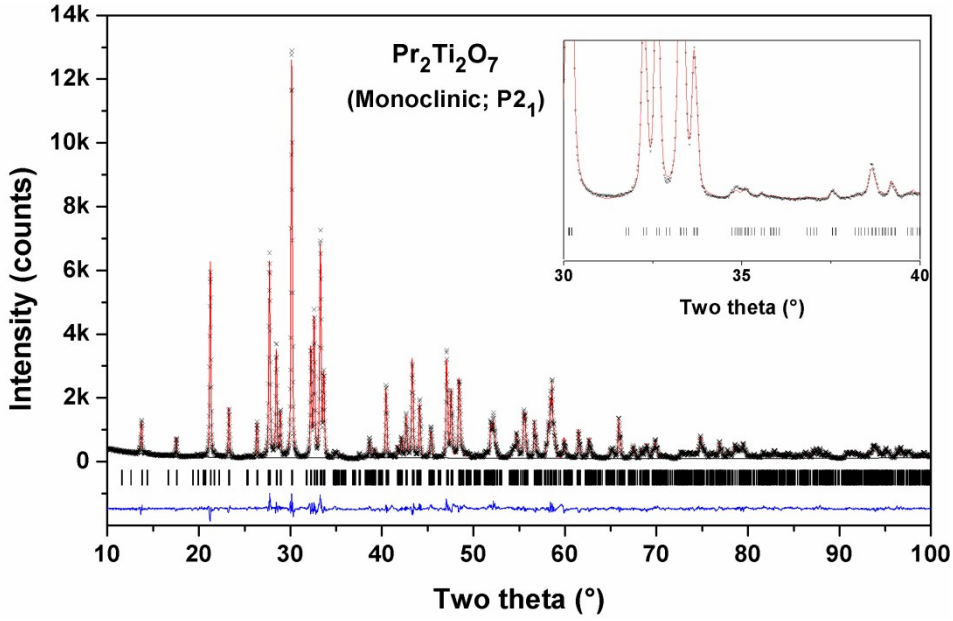

Figure 2: Rietveld refinement plot of $Pr_2Ti_2O_7$ in $P2_1$ model.

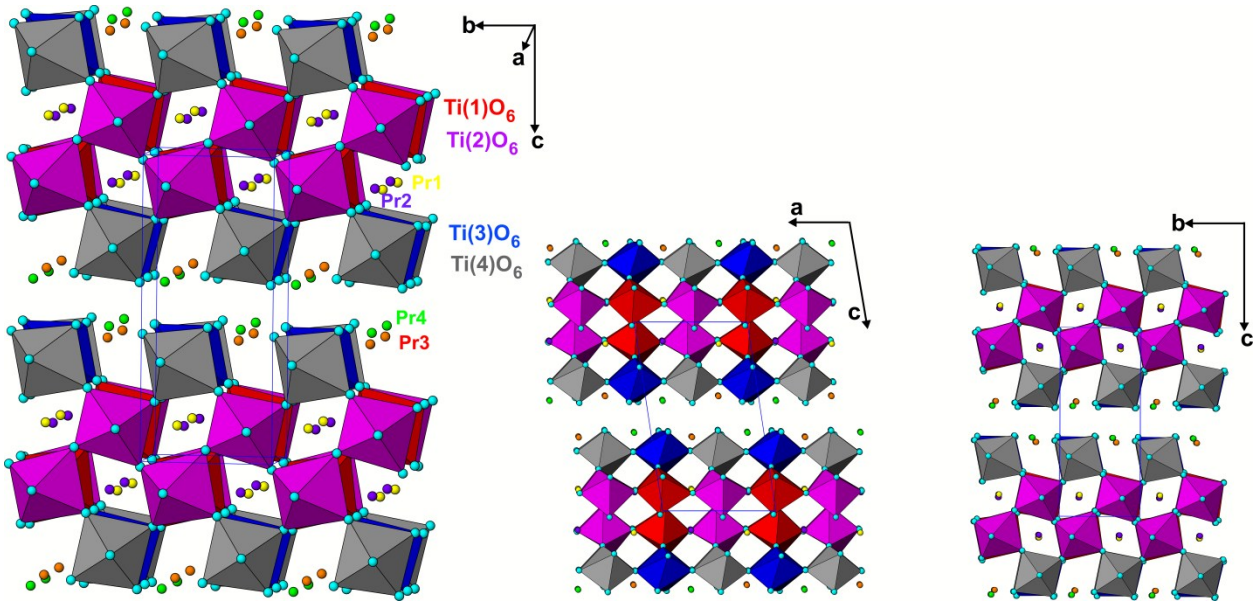

Figure 3: Crystal structure of $Pr_2Ti_2O_7$ in different projection (TiO_6 octahedra are shown, isolated spheres are Pr atoms).

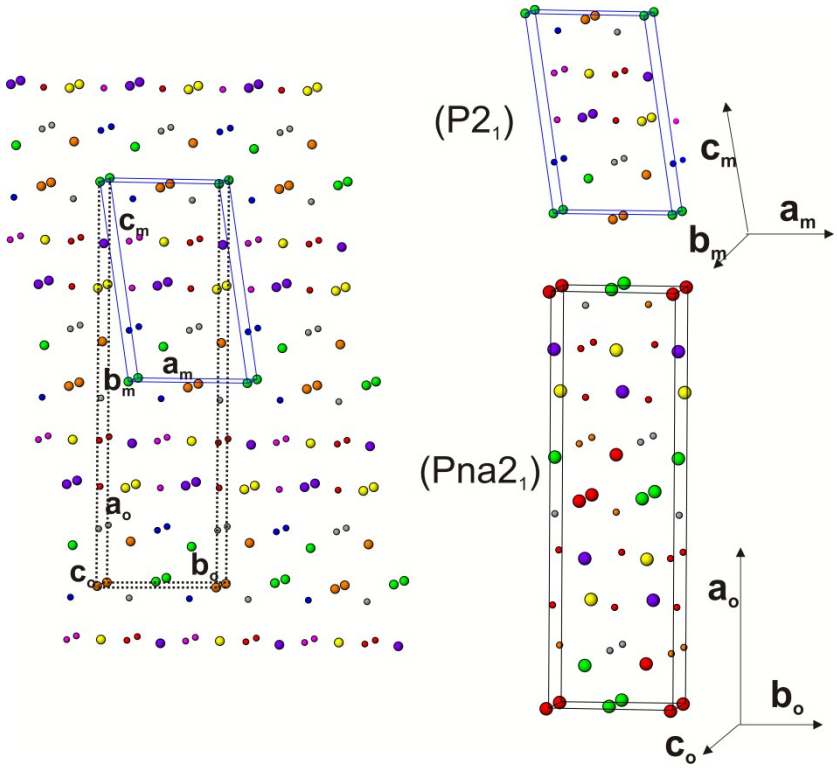

Figure 4: Comparison of monoclinic $P2_1$ and orthorhombic $Pna2_1$ structures of $Pr_2Ti_2O_7$. Only cations are shown (Larger sphere: Pr^{3+} and Small sphere: Ti^{4+}). The unit cell are related as: $a_o = 2c_m cos(\beta\text{-}90)$, $b_o = a_m$, $c_o = b_m$.

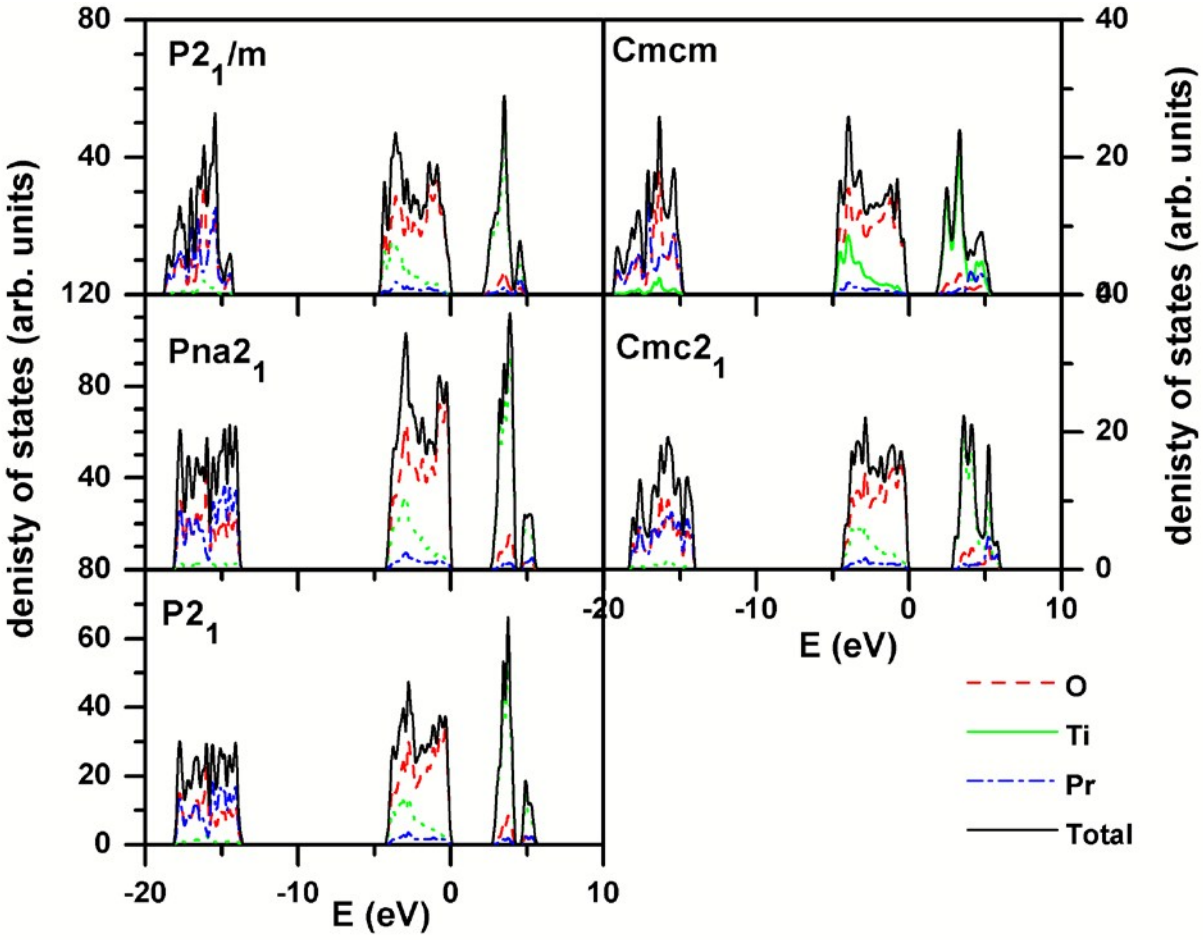

Figure-5: Calculated density of states of $Pr_2Ti_2O_7$ for different structures. (For $P2_1$, $Pna2_1$ and $Cmc2_1$ model, the band gaps are similar (~2.7 eV) while for the paraelectric Cmcm and $P2_1/m$, the band gaps have lower values (~ 2 eV).

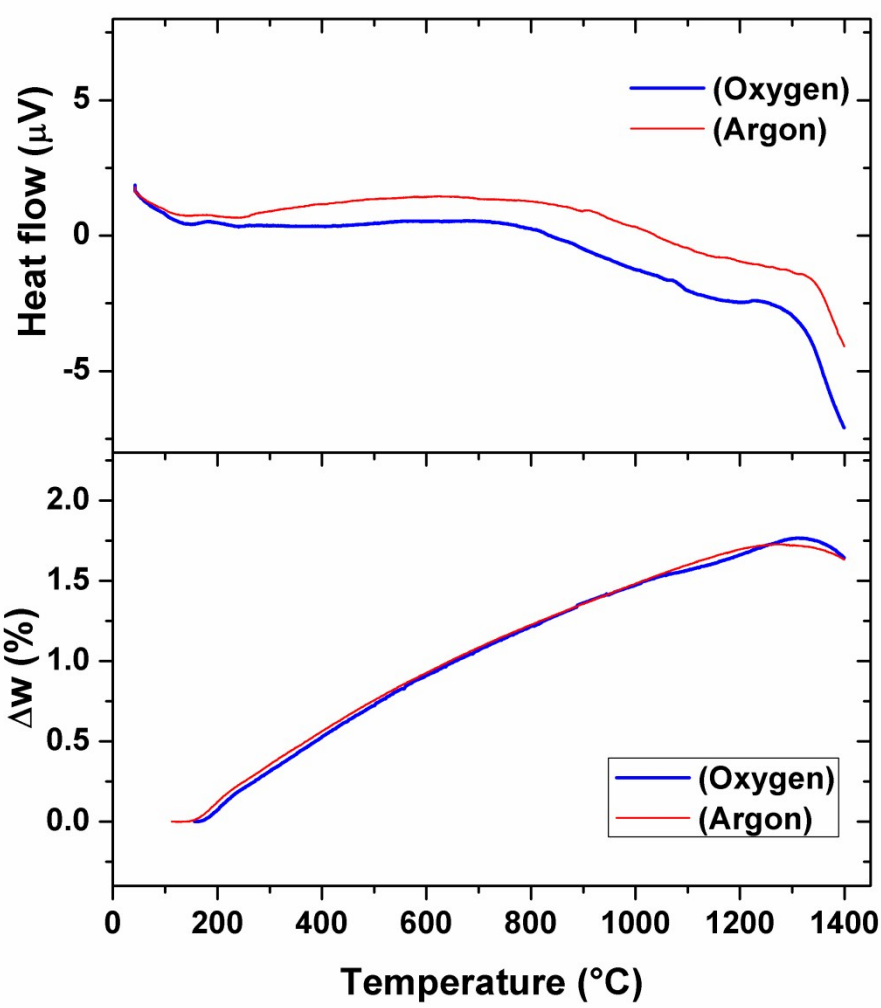

Figure 6: TG/DTA curves of $Pr_2Ti_2O_7$ while heating from ambient to 1673K. (Heating rate = 10 K/min).

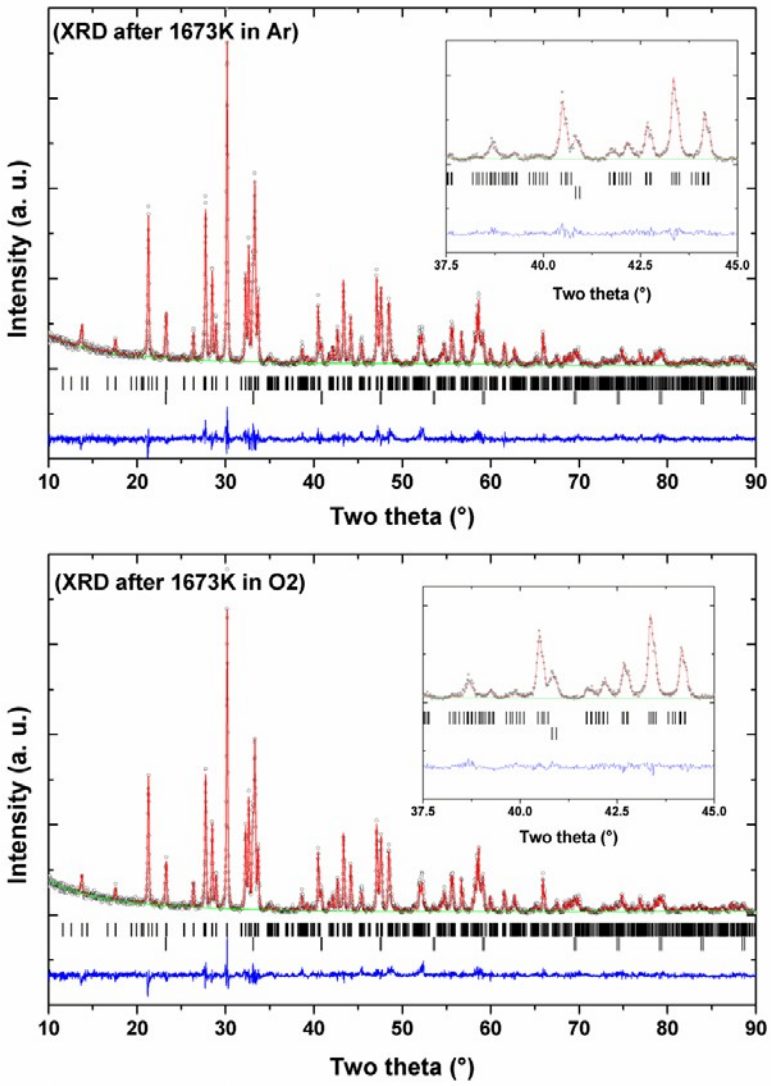

Figure 7: XRD patterns of $Pr_2Ti_2O_7$ recorded after heating at 1673K in argon and oxygen atmosphere

(Argon) : a = 7.7158(2) Å, b = 5.5878(2)Å, c = 13.0031(4) Å, β = 98.572(6)°, V = 544.43(2) Å^3. R_p = 9.78 %, R_{wp} = 12.9 % and χ^2 = 1.749

(Oxygen): a = 7.7159(2) Å, b = 5.5878(2) Å, c = 13.0021(3) Å, β = 98.582(4)°, V = 544.39(2) Å^3. Rp = 9.63 %, Rwp= 12.7 % and χ^2 = 1.884

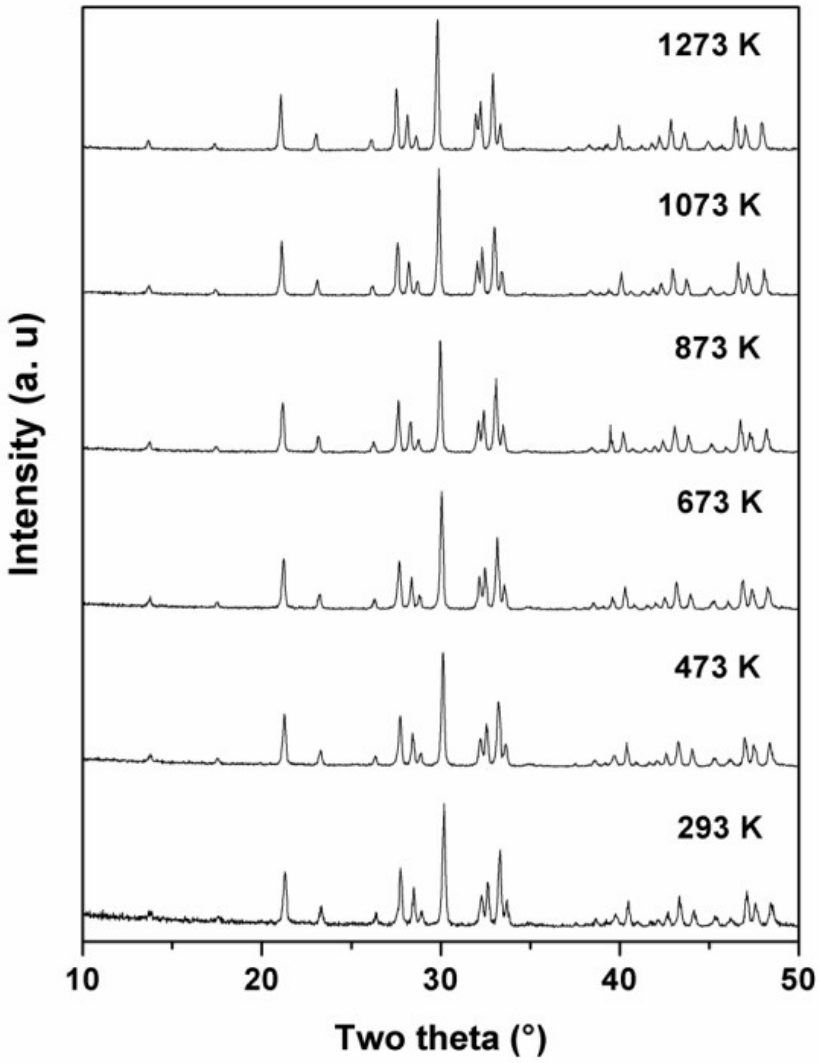

Figure 8: Typical powder XRD patterns of PTO recorded at different temperatures.

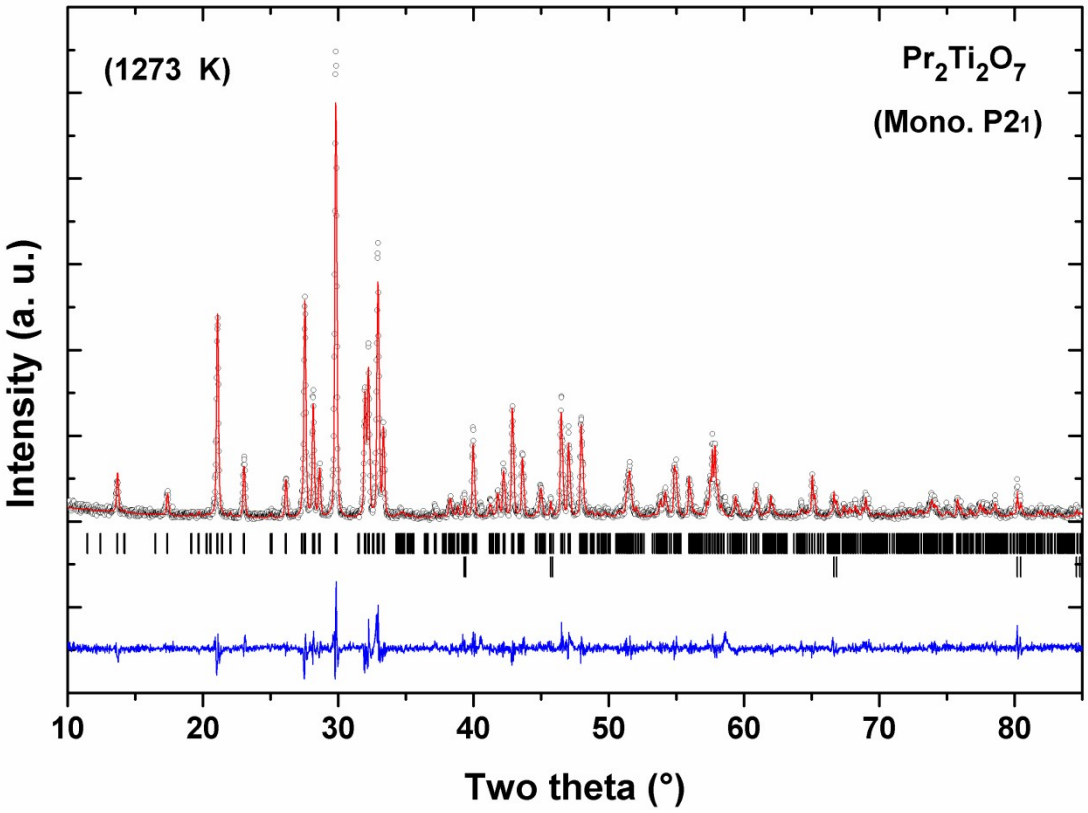

Figure 9: Typical Rietveld refinement plot of XRD data of $Pr_2Ti_2O_7$ recorded at 1273 K. (Lower vertical ticks indicate Bragg position (upper panel: $Pr_2Ti_2O_7$ and Lower panel: sample holder). (Rp = 15.7 %, Rwp = 20.8 %, $\chi 2 = 1.67$)

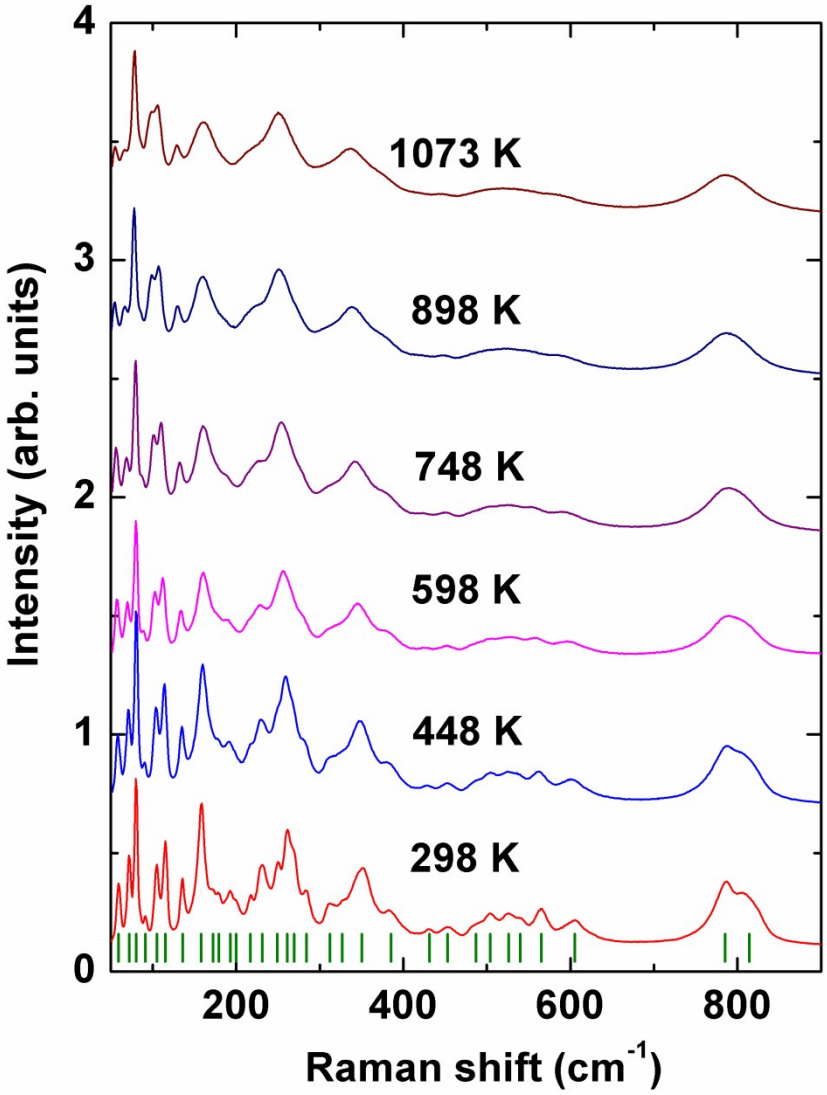

Figure 10: Raman spectra of $Pr_2Ti_2O_7$ at different temperatures. Vertical bars show the positions of Raman modes.

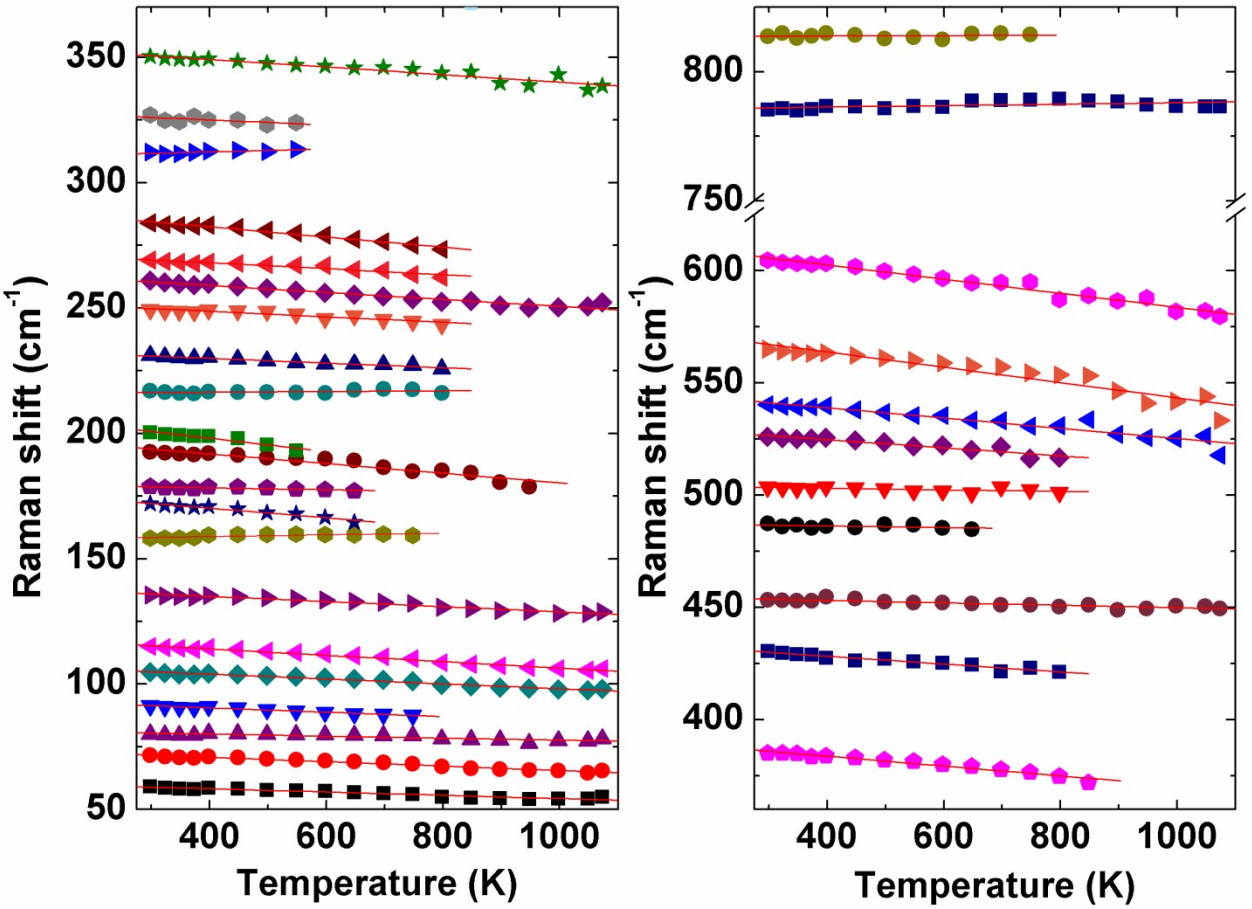

Figure 11: Temperature dependence of Raman mode frequencies of $Pr_2Ti_2O_7$.

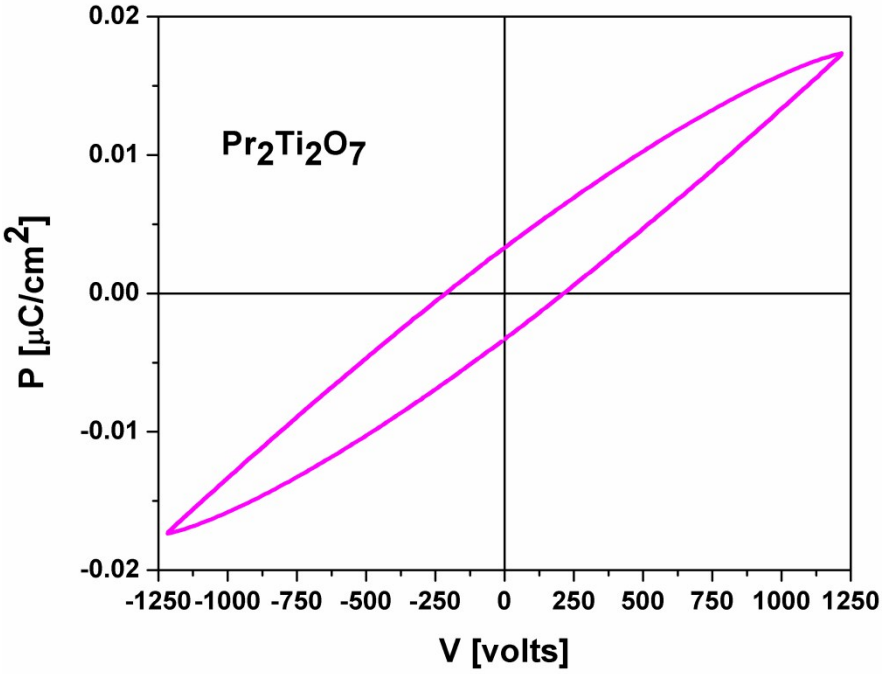

Figure 12: Ambient temperature PE loops of $Pr_2Ti_2O_7$.

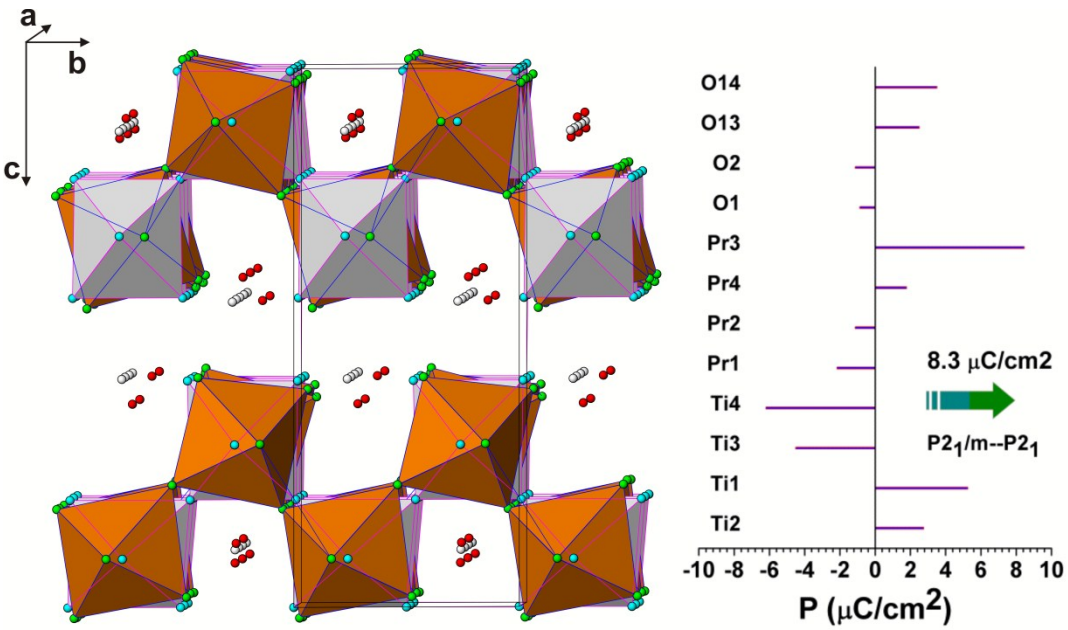

Figure 13: Comparison of monoclinic ferroelectric $P2_1$ and paraelectric $P2_1/m$ structures of $Pr_2Ti_2O_7$. Light shades: $P2_1/m$ structure and colour: $P2_1$ structure. The spontaneous polarizations along b-axis due to shift of various ions are shown in right hand side figure.

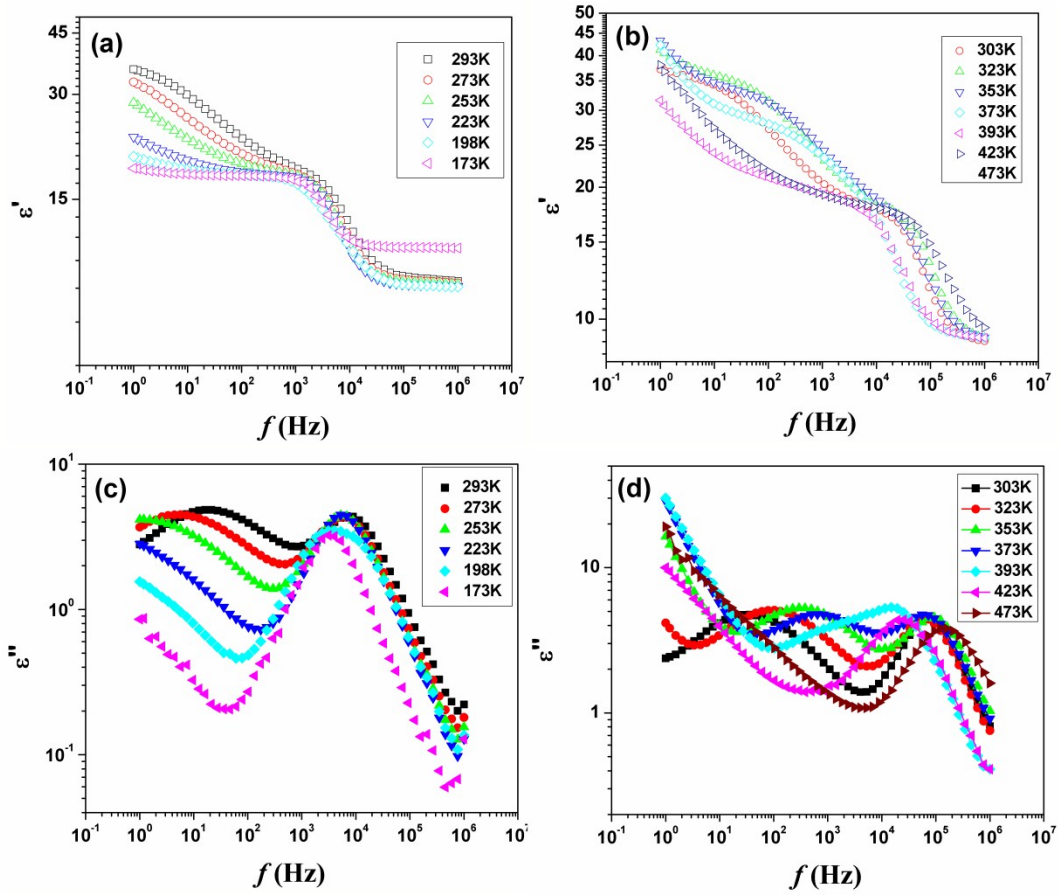

Figure 14: Temperature dependent ε'(a and b) and ε'' (c and d) of $Pr_2Ti_2O_7$in low temperature region.

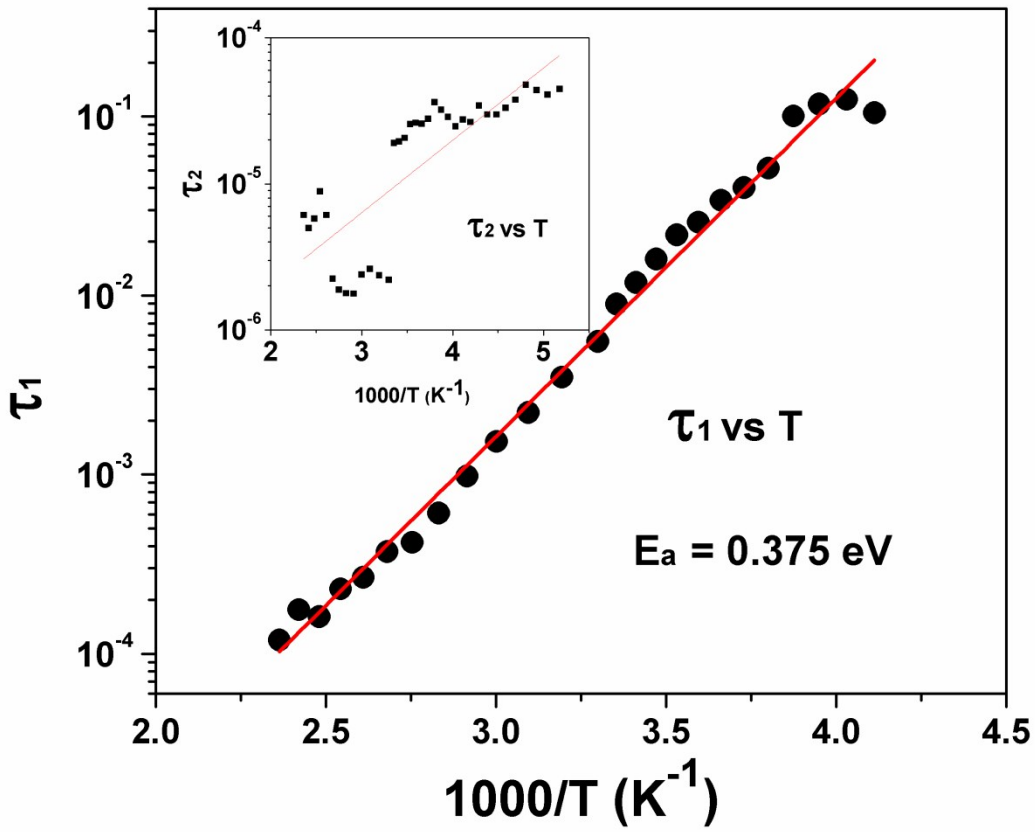

Figure 15: Typical Arrhenius fit for low temperature relaxation (τ_1) of $Pr_2Ti_2O_7$. The temperature dependency of τ_2 is shown as inset.

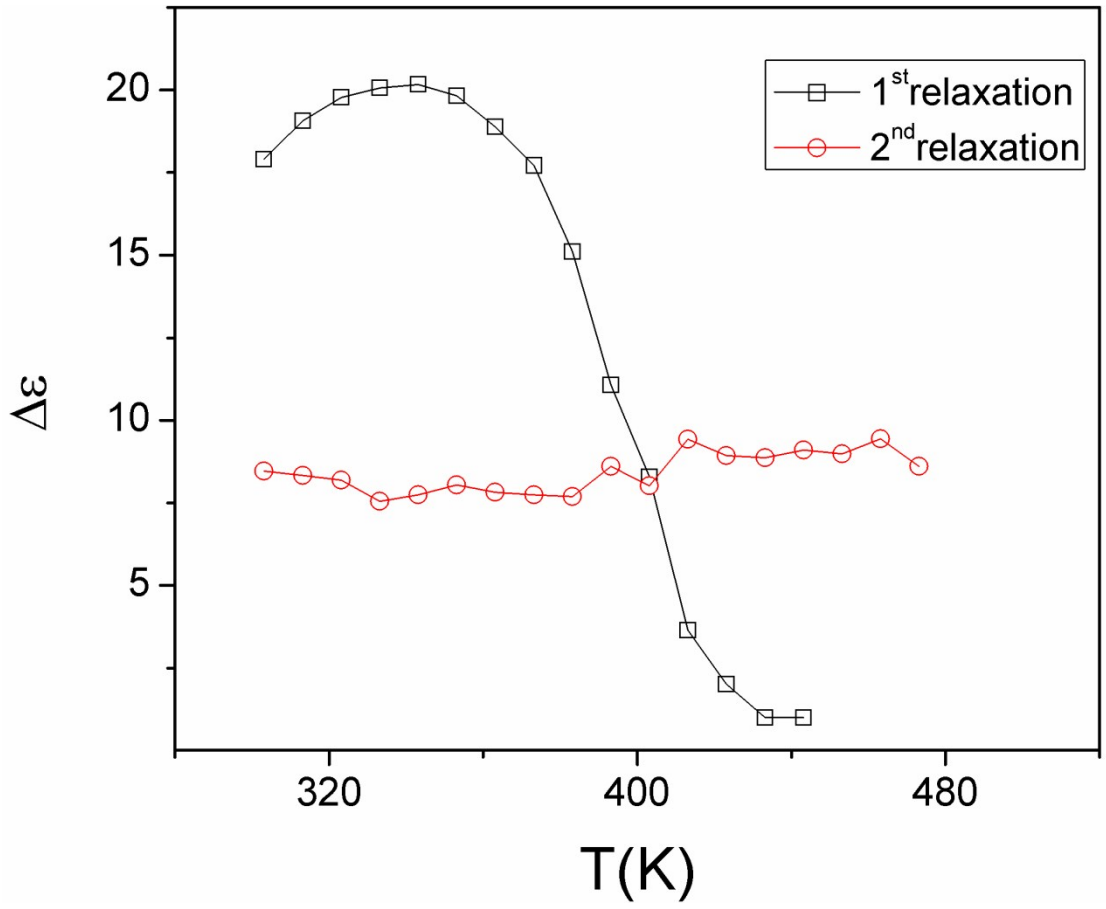

Figure 16: Variation of dielectric strength of the two low temperature relaxations of $Pr_2Ti_2O_7$ with temperature.

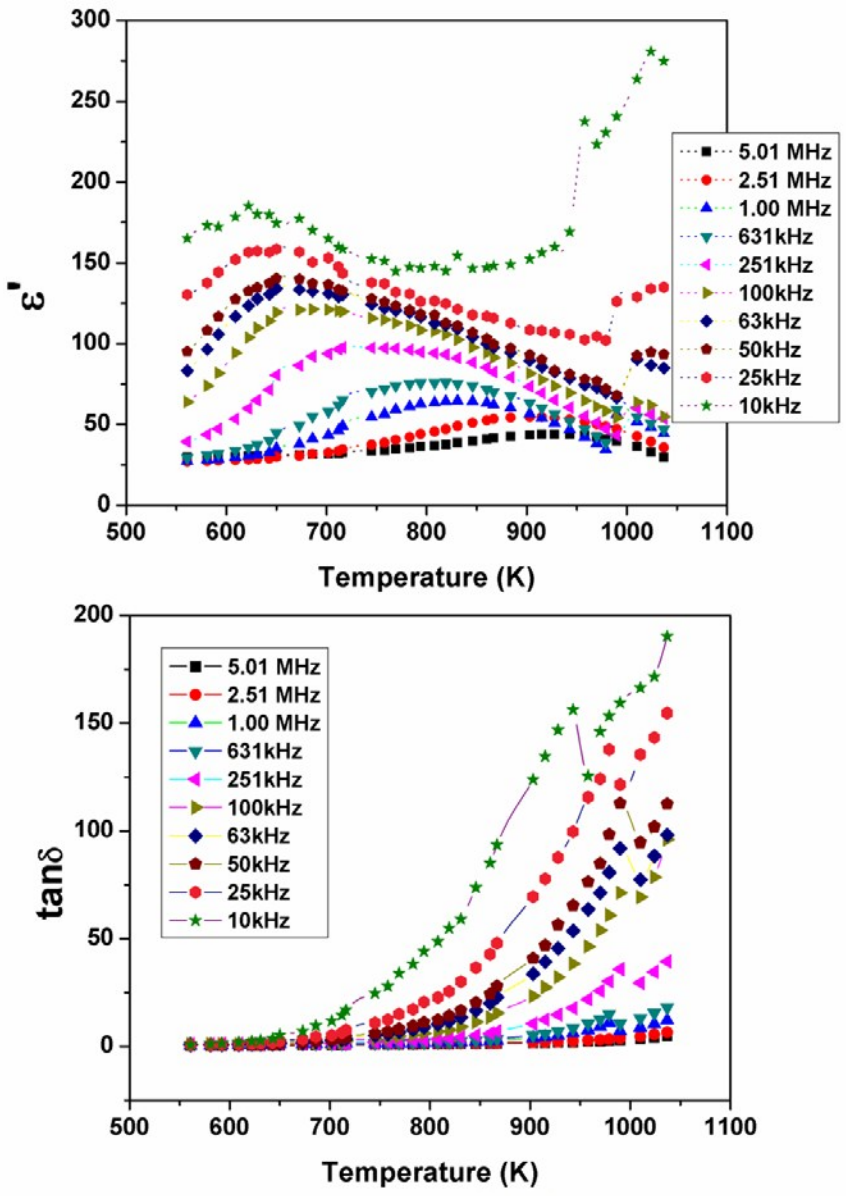

Figure 17: Temperature dependent ε' and *tanδ* of $Pr_2Ti_2O_7$ at selected frequencies in high temperature region.

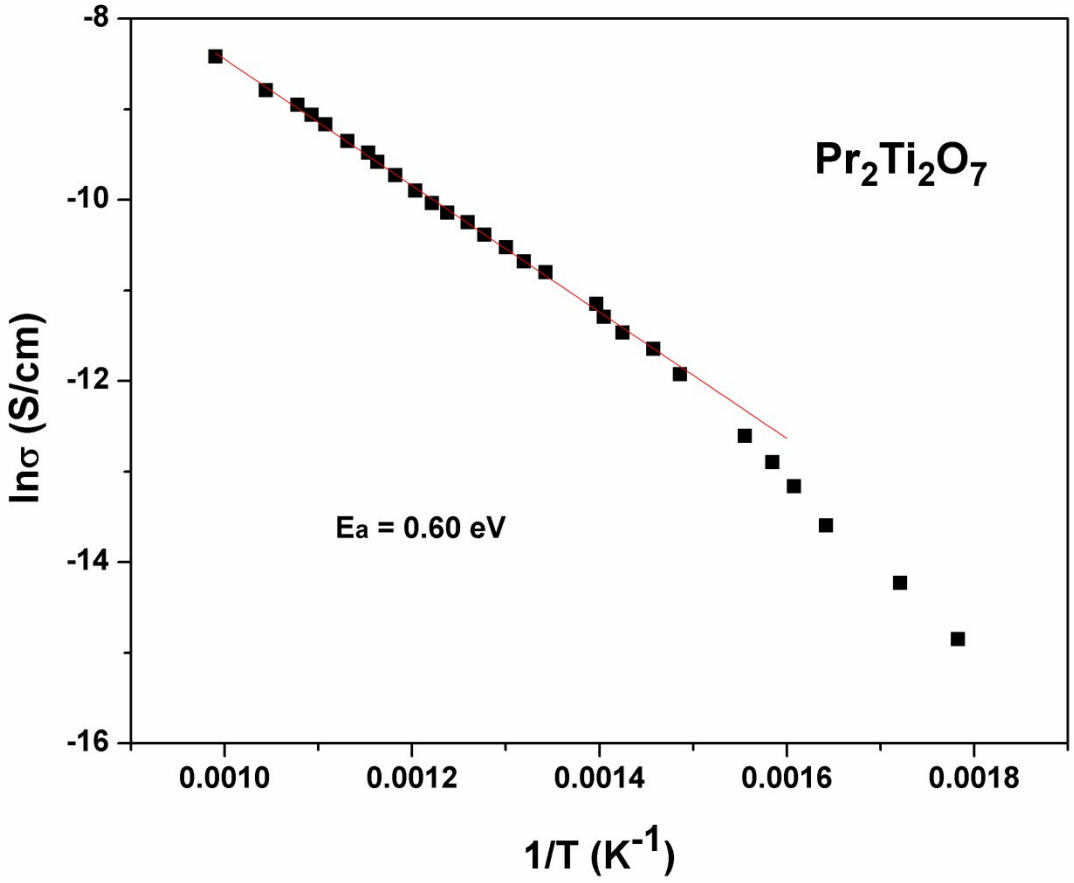

Figure 18: Variation of total conductivity of $Pr_2Ti_2O_7$with temperature at high temperature (Arrhenius fits are shown as solid line).

Figure for TOC